








EX LIBRIS  
UNIVERSITATIS  
ALBERTENSIS

---

The Bruce Peel  
Special Collections  
Library





Digitized by the Internet Archive  
in 2025 with funding from  
University of Alberta Library

<https://archive.org/details/0162014674681>









**University of Alberta**

**Library Release Form**

**Name of Author:** Steven David Thomas

**Title of Thesis:** Transient Magnetization Magnetic Resonance Angiography at 3.0 Tesla

**Degree:** Master of Science

Permission is hereby granted to the University of Alberta Library to reproduce single copies of this thesis and to lend or sell such copies for private, scholarly, or scientific research purposes only.

The author reserves all other publication and other rights in association with the copyright in the thesis, and except herein before provided, neither the thesis nor any substantial portion thereof may be printed or otherwise reproduced in any material form whatever without the authors prior permission.





**University of Alberta**

**Transient Magnetization Magnetic Resonance Angiography  
at 3.0 Tesla**

by

**Steven David Thomas**



A thesis submitted by the Faculty of Graduate Studies and Research in  
partial fulfillment of the requirements for the degree of Master of Science

Department of Biomedical Engineering

Edmonton, Alberta

Fall 2001





**University of Alberta**

**Faculty of Graduate Studies and Research**

The undersigned Certify that they have read, and recommend to the Faculty of Graduate Studies and Research for acceptance, a thesis entitled **Transient Magnetization Magnetic Resonance Angiography at 3.0 Tesla** by **Steven David Thomas** in partial fulfillment of the requirement for the degree of **Master of Science**





For my Mom, Dad and Sister, thank you.



# Abstract

Two techniques for three-dimensional (3D) Magnetic Resonance Angiography (MRA) at 3.0 T were developed and tested on normal volunteers at 3.0 T. Although quite different, both techniques rely on the exploitation of time-varying magnetization in 3D MRA. In the first case, it is the recovery of background signal following pulsed magnetization transfer that is exploited, while in the second case, it is the decay of blood signal following rapid, repeated excitation within a segmented acquisition.

In the first case, magnetization transfer (MT) was applied in three-dimensional time-of-flight magnetic resonance angiography (MRA) at 3.0 T for imaging the intracranial arteries. By using a modulated MT approach and an altered phase encode order, the specific absorption rate was kept below 3 W/kg over any 8 s time period. For a 20° flip angle and 36 ms repetition time, the background suppression at 3.0 T was improved with MT by  $52 \pm 5\%$  for white matter and  $40 \pm 8\%$  for grey matter, making the distal intracranial vasculature significantly more discernible.

In the second case, cardiac triggered Magnetization Prepared (MP) MRA with venous suppression and fat saturation was applied at 3.0 T for imaging of the carotid arteries. Signal-to-noise gains and longer inflow times at 3.0 T were advantageous over performing the scan at 1.5 T. The technique was compared to time-of-flight MRA giving improved background suppression of  $71\% \pm 6\%$ .





# Acknowledgments

First and foremost I would like to acknowledge and thank my supervisor Dr. Alan H. Wilman for his help in all things relating to this project and my scientific career. If there has been a single correct decision made in my postgraduate education it has been my choice of supervisor. He has been extremely selfless in regards to my development in this field and has made an excellent and much appreciated mentor. I would like to thank Dr. Derek Emery for his reminders as to what the physics was actually supposed to accomplish, for his scaring me into learning cranial vasculature and for teaching me (the hard way) that I am not so hot at squash. I would also like to thank Dr. Richard Snyder for his support of my ideas, knowledge about triggering devices, and his practical knowledge of how to obtain a masters degree.

I would like to thank Dr. Jim Wild who helped me a great deal in overcoming the NMR learning curve. Besides his mentoring he has been a valued friend, climbing partner and roommate. I also greatly appreciate Dr. Peter Allen for his flexibility in course scheduling and his depth of understanding of both NMR and Tim Hortons as a Canadian institution. Dr Christian Beaulieu has helped in my understanding of MT and is the backbone of the Edmonton BME pool team.

I would like to thank the staff at the NMR facility. Dr. Chris Hanstock for his knowledge of all T1's encountered and Dan Georghiu for keeping me in business after I have thoroughly abused the gradient amplifiers. I would like to thank Carol Tymchuk and Maisie Goh for often feeding me lunch and Brenda Carrier for monthly feeding me desert. Further more I would like to thank the computer guys Shuan and Beau for their help in all things computer related.

I am in great appreciation of my Edmonton companions Mike Mercier, Chris Huisman, Jorge Parada Perez and Mike Orr who along with Megan (Jelly Bean) Huston (honorary Edmontonian) are treasured friends, confidants, room mates and lab rats. I would further like to acknowledge the rest of my surrogate family and fellow gypsies, Denny Winkleberry, Markus Bradey, Willi, Juan Dog, Evil Conevil, Brad Gom, Dugly, Nadia, Ainslberri, Yodi, Ham Solo and the infamous Foroud sisters Nora Borealis and mighty Afrodite who are all much loved.

I would also like to thank Amy Thorpe who is a tireless discussion partner on all topics under the sun, a valued confidant and who is very dear to me.

I would like to thank Osama, Nick and Zaki for the help received in the writing of this thesis and their friendship.

I would also like to acknowledge the other students within NMR, Atiyah, Kim, Jason, Morgan, Keith, Rich, Jeff and Alison who are all super fun and kinda funny. Though not ha ha funny.



I would like to thank Paul & Evelyn Huisman for both their wonderful company and the home cooked meals they have provided me.

I would like to thank Val and Moe for providing me with ample supplies of the will power you just cannot get from digging deep. I am talking about the medium roasted, highly caffeinated and very sugary kind of will power only found in the finest of coffee bars that makes thesis writing possible.

I would like to thank my sister Sarah for being supportive in all the ways families and friends are supportive. I should also mention that she played a large role in the acquiring of volunteers during the pulse sequence development phase and is much appreciated for her effort.

Finally I would like to acknowledge my parents Louise and Julian Thomas who have provided both support and freedom from day one. Thank you and I love both of you.





# Table of Contents

## Chapter 1: Introduction and Background

1.1 Introduction	1
1.2 The Quantum Mechanical Description of NMR	2
1.21 Spin $\frac{1}{2}$ in a static magnetic field of strength $B_0$	2
1.3 The classical description of NMR	5
1.31 Magnetic moments in a stationary magnetic field $B_0$	5
1.32 Magnetic moments in a stationary magnetic field and a radio frequency (RF) circularly polarized magnetic field $B_1(t)$	9
1.4 Relaxation mechanisms as contrast mechanisms and the Bloch equations	15
1.41 Longitudinal Relaxation	15
1.42 Transverse Relaxation	18
1.5 Spatial Encoding	20
1.51 Slice Selection	21
1.52 Frequency Encoding	22
1.53 Phase Encoding	23
1.54 Radio Frequency (RF) excitation pulses	25
1.6 The Signal Equation and k space	27
1.7 Other Methods of Tissue Contrast	31
1.71 Fat Suppression	31
1.72 Magnetization Transfer (MT)	32
1.8 Power Deposition and the Specific Absorption Rate (SAR)	34
1.9 References	37

## Chapter 2: Standard Time-of-Flight MR Angiography

2.1 Introduction	39
2.2 Two-dimensional vs. Three-dimensional MRA	41
2.3 The 3D TOF MRA pulse sequence	43
2.31 Venous Suppression and the Saturation Pulse	44
2.32 Excitation and the Ramp Pulse	45
2.33 Flow Compensation	46
2.34 Suppression of Fat signal & Echo Time.	47
2.4 References	49



## **Chapter 3: Modulated Magnetization Transfer TOF MRA**

<b>3.0 Introduction</b>	<b>51</b>
<b>3.1 Materials and Methods</b>	<b>52</b>
<b>3.2 Results</b>	<b>56</b>
<b>3.3 Discussion</b>	<b>61</b>
<b>3.4 References</b>	<b>63</b>

## **Chapter 4: Magnetization-Prepared Time of Flight MR Angiography**

<b>4.0 Introduction</b>	<b>65</b>
<b>4.1 MP FLASH Sequence</b>	<b>67</b>
<b>4.2 Magnetization Preparation and Signal Suppression</b>	<b>68</b>
4.21 Inversion Pulse and Tissue Suppression	69
4.22 Venous Suppression.	72
4.23 Fat Saturation	74
<b>4.3 Imaging with FLASH (k space sampling)</b>	<b>75</b>
4.31 Minimizing flow dephasing through short TE	76
4.32 K space Modulation and Center Out Slice-Phase Encode Order	78
4.33 Modulated Flip Angle for Modulating k Space	80
<b>4.4 Cardiac Triggering</b>	<b>82</b>
4.41 Maximizing the T1 Advantage and the Two Heart Beat Acquisition	83
4.42 Method of Cardiac Triggering (Electric vs Fiber Optic Leads)	85
4.43 Positioning of the inversion pulse and acquisition	87
<b>4.5 Comparison of MP TOF with Standard TOF</b>	<b>89</b>
<b>4.6 Discussion</b>	<b>94</b>
<b>4.7 References</b>	<b>96</b>

## **Chapter 5: Conclusion**

<b>5.1 Conclusions</b>	<b>100</b>
<b>5.2 Future Directions</b>	<b>101</b>





# List of Tables

## Chapter 1

1-1	T1's at 1.5 T and 3.0 T field strengths for various tissues	17
1-2	T2's for various brain constituents at 1.5 T	20

## Chapter 3

3-1	Intracranial vessel blood to background measurements at 1.5 T and 3.0 T	60
-----	--	----

## Chapter 4

4-1	SNR, CNR , C and BNR for both MP MRA on TOF MRA at 3.0 T	90
4-2	Percent change between TOF MRA and MP MRA at 3.0 T	90



# List of Figures

## Chapter 1

1-1	Splitting of energy levels in an external magnetic field	4
1-2	Classical vector representation of protons in a magnetic field	6
1-3	Clockwise precession of a protons magnetic moment about the magnetic field $B_0$	8
1-4	The rotating frame of reference with respect to the laboratory frame	12
1-5	Motion of the magnetic moment in rotating reference frame in the presence of $B_{\text{eff}}$	12
1-6	Motion of the magnetization vector during a 90 degree pulse shown in both the rotating and laboratory reference frames	14
1-7	The time-dependent emf signal resulting from the precession of the magnetic moment and the resulting power spectrum	15
1-8	Longitudinal magnetization re-growth for different tissues and excitation flip angles	18
1-9	Loss of coherent signal due to fluctuating $\omega_0$	20
1-10	Phase distribution before and after the application of the phase gradient $G_y$ for time $t_y$	25
1-11	Bandwidth for a given RF pulse	26





1-12	Temporal and Frequency relationships for given hard and soft pulses	27
1-13	K space sampling for 2D gradient echo pulse sequence	29
1-14	Frequency separation of water and fat	32
1-15	Power spectrum for bound and freely moving protons	34

## Chapter 2

2-1	TOF imaging for flowing and steady state signal	41
2-2	Timing diagram for a 3D TOF MRA sequence	43
2-3	Positioning of venous saturation and imaging slabs for intracranial MRA	44
2-4	Effect of a ramp excitation pulse on tissue and blood	45
2-5	Relative phase of water and fat at different TE's	48

## Chapter 3

3-1	Timing diagram for the 3D TOF MRA pulse sequence	53
3-2	Phase encode order for the 3D pulsed MT TOF MRA sequence	54
3-3	MT pulse amplitude, signal profile and average power deposition for 256 views of single $k_y$ pass of k-space	57



3-4	Source images acquired with and without pulsed MT showing differences in background suppression	58
3-5	Source images acquired with and without pulsed MT showing relative differences in signal variation across the imaging slab	59
3-6	Collapsed images acquired with and without MT at 1.5 T and 3.0 T showing relative background suppression	61

## Chapter 4

4-1	Blood and background longitudinal magnetization during an MP MRA pulse sequence	66
4-2	Magnetization preparation and imaging component play out for segmented acquisition	67
4-3	Timing diagram for the MP component of the 3D MP MRA pulse sequence	68
4-4	Source images showing the effect of different inversion times	70
4-5	Graph showing the signal vs inversion time at $B_0=1.5T$ and $3.0T$	71
4-6	Source image with venous suppression	73
4-7	Spectra showing fat suppression	74
4-8	Collapsed images showing fat suppression	75





4-9	Timing diagram for the imaging component of the 3D MP MRA pulse sequence	76
4-10	Truncated Sinc pulse for the reduction of TE	77
4-11	Respective image profiles for sequential and center out phase encodes	79
4-12	Respective image profiles for steady states and variable flip angles	82
4-13	Optimum null times for various heart rates	84
4-14	EKG waveforms inside and outside of the magnet	85
4-15	PO waveforms inside and outside the magnet	86
4-16	MP MRA source images acquired with and without gating	88
4-17	Source images comparing TOF MRA and MP MRA	92
4-18	Source images comparing TOF MRA and MP MRA	93



# SYMBOLS

$\mathbf{B}_0$	external magnetic field
$\mathbf{B}_1$	radio frequency magnetic field
$\mathbf{B}_{\text{eff}}$	effective magnetic field
$\text{BW}_{\text{rec}}$	receiver bandwidth
$\text{BW}_{\text{rf}}$	RF bandwidth
$C$	normalized contrast
$E$	Interaction energy
$\text{FOV}_y$	field of view in the phase direction
$\text{FOV}_x$	field of view in the read direction
$G_d$	gradient in arbitrary direction
$G_x$	readout gradient
$G_y$	phase encoding gradient
$G_{y\text{inc}}$	phase encoding gradient increment
$G_z$	slice select gradient
$H_b$	protons from bound water molecules
$H_f$	protons from free water protons
$\mathbf{I}$	spin angular momentum
$k$	Boltzman's constant
$\mathbf{M}_0$	net magnetization vector
$M_x$	transverse X magnetization



$M_{xy}$	transverse magnetization
$M_y$	transverse Y magnetization
$M_z$	longitudinal magnetization
$N_{\text{freq}}$	number of acquisitions in the frequency encode direction
$N_{\text{pe}}$	number of phase encoding steps (Y direction)
$N_{\text{pe slice}}$	number of phase encoding steps (Z direction)
SNR	signal to noise ratio
T	absolute temperature
TE	echo time
TR	repetition Time
T1	longitudinal relaxation time
T2*	transverse relaxation time (reversible & nonreversible)
T2'	transverse relaxation time (reversible)
T2	transverse relaxation time (nonreversible)
$T_{\text{inv}}$	inversion time
$T_{\text{null}}$	null time
$TH_{\text{slice}}$	slice thickness
$TH_{\text{slab}}$	slab thickness
$T_{\text{sat}}$	delay time after the saturation pulse
$v_x$	constant velocity of spins
$x_o$	initial position of spins
$\Delta y$	spatial resolution in Y direction
$\Delta x$	spatial resolution in X direction





$\Delta k_x$	sampling period in $k_x$ -space
$\Delta k_y$	sampling period in $k_y$ -space
$\Delta t$	sampling intervals
$\alpha$	flip angle
$\Theta$	phase
$\hbar$	Planck constant divided by $2\pi$
$\mu_x$	X component of magnetic moment
$\mu_y$	Y component of magnetic moment
$\mu_z$	Z component of magnetic moment
$\mu$	magnetic dipole moment
$\gamma$	proton gyromagnetic ratio
$\omega_0$	Larmor frequency (resonance frequency)
$ \alpha\rangle$	Parallel spin
$ \beta\rangle$	Anti-parallel spin



# Abbreviations

BW	Bandwidth
C	Normalized Contrast
CNR	Contrast to Noise Ratio
EMF	Electromotive Force
FOV	Field of View
MCA	Middle Cerebral Artery
MOTSA	Multiple Overlapping Thin Slice Acquisition
MP	Magnetization Prepared
MRA	Magnetic Resonance Angiography
MRI	Magnetic Resonance Imaging
MT	Magnetization Transfer
NMR	Nuclear Magnetic Resonance
RF	Radio Frequency
ROI	Region of Interest
SAR	Specific Absorption Rate
SNR	Signal to Noise Ratio
TE	Echo Time
TOF	Time of Flight
TR	Repetition Time
2D	Two Dimensional
3D	Three Dimensional



# CHAPTER 1

## Introduction and Background

### 1.1 Introduction

The development of magnetic resonance imaging (MRI) over the last quarter century has resulted in a robust modality for the imaging of soft tissue and fluids in vivo. Magnetic resonance imaging involves the spatial localization of signal from the nuclear magnetic resonance (NMR) experiment, which gives MRI a great number of contrast mechanisms ranging from magnetic properties of tissues to molecular motion. These contrast mechanisms make MRI an extremely flexible imaging modality and useful tool in the diagnosis of many of the pathologies.

This thesis deals with research into an area of MRI known as Magnetic Resonance Angiography (MRA), which is used for imaging blood vessels. Before studying MRA specifically, it is necessary to understand the principles of MRI. Similarly, to understand MRI, it is necessary to understand first the physical principals that underlie the basic NMR experiment then secondly the principles of spatial encoding.

This chapter is presented as a brief overview of some of the fundamentals of NMR phenomena as well as the techniques required to spatially encode the NMR signal. A more in-depth description of the topics presented here can be found in the references [1-4].





## 1.2 The Quantum Mechanical Description of NMR

### 1.21 Spin $\frac{1}{2}$ in a static magnetic field of strength $B_0$

Nuclei have an associated magnetic dipole moment of  $\mu$  which is related to the spin angular momentum operator of the nuclei  $\mathbf{I}$  through the equation:

$$\mu = \gamma \hbar \mathbf{I} \quad (1-1)$$

where  $\gamma$  is the gyromagnetic ratio of the associated nuclei, which has the units of frequency over magnetic field and  $\hbar$  is Plank's h constant divided by  $2\pi$  having the value of ( $\hbar = 1.054 \times 10^{-34}$  J.s). In the case of the hydrogen proton which is our nuclei of interest  $\gamma = 42.7$  MHz/Tesla.

The interaction energy of a magnetic moment in a magnetic field  $\mathbf{B}$  is defined by:

$$E = -\mu \cdot \mathbf{B} \quad (1-2)$$

In the case of single hydrogen nuclei ( $I = \frac{1}{2}$ ) in a static uniform magnetic field  $\mathbf{B}_0$  orientated in the Z direction of the Cartesian frame the equation for interaction becomes:

$$E = -\gamma \hbar \mathbf{I}_z \cdot \mathbf{B}_0 \quad (1-3)$$



Rearranging the equation into operator form we get the Zeeman Hamiltonian operator:

$$\mathcal{H}B_0 = -\gamma\hbar B_0 \mathbf{I}_z \quad (1-4)$$

If we apply the Zeeman Hamiltonian operator to the energy eigenstates in the spin wave function we get the corresponding energy eigenvalues of those corresponding eigenstates defined by:

$$\mathcal{H}_{B_0} (|\alpha\rangle + |\beta\rangle) = E (|\alpha\rangle + |\beta\rangle) = \gamma\hbar B_0/2 |\alpha\rangle + -\gamma\hbar B_0/2 |\beta\rangle \quad (1-5)$$

where  $|\alpha\rangle$  are spins orientated parallel to  $\mathbf{B}_0$  and  $|\beta\rangle$  are spins orientated anti parallel to  $\mathbf{B}_0$ . Thus when one spin  $\frac{1}{2}$  system is placed in a static magnetic field there are two possible energy states in which any spin can be described as an admixture of both if not purely one or the other state [5].

The Zeeman energy can also be written:

$$\Delta E = \hbar \omega_0 \quad (1-6)$$

And thus:



$$\omega_0 = \gamma B_0 \quad (1-7)$$

where  $\omega_0$  is referred to as the Larmor frequency.

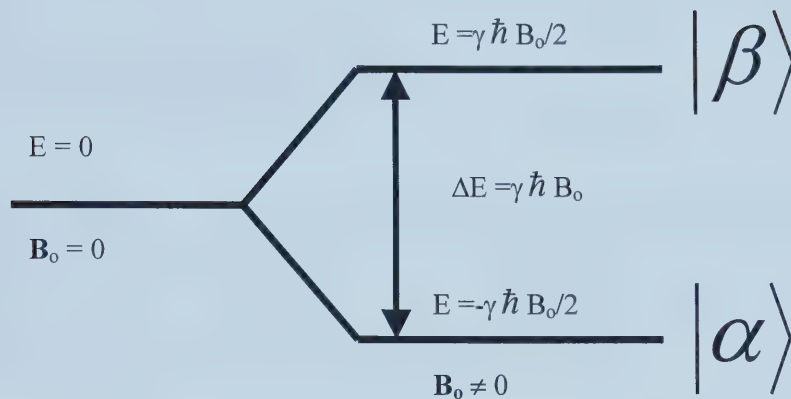


*Figure 1-1*

*The energy level diagram of a spin  $\frac{1}{2}$  system moved from a magnetic field of  $B_0 = 0$  to a magnetic field of  $B_0 \neq 0$*

In thermal equilibrium the relative populations of spins in each eigenstate is determined by the Boltzman distribution [2] which may be expressed as:

$$N_{|\beta\rangle} / N_{|\alpha\rangle} = e^{-\Delta E/kT} \quad (1-8)$$

where  $N$  represents the spin populations in the respective eigenstate,  $k$  is the Boltzman constant  $k = 1.38 \times 10^{-23}$  J/K and  $T$  is the temperature in units of Kelvin.





In the absence of a magnetic field, the probability of a spin being orientated in any direction is equal, however a spin in the presence of a static magnetic field will preferentially orient itself parallel to the field. This preference of spins toward the parallel state results in the net longitudinal magnetisation of the sample.

### **1.3 The classical description of NMR**

Consider an arbitrary sample volume containing an ensemble of protons each with an individual magnetic moment of  $\mu$ . The net magnetisation of the sample results from the sum of the magnetic moment vectors within the sample:

$$\mathbf{M}_0 = \sum_{\text{Volume}} \mu_i \quad (1-10)$$

In the absence of a magnetic field these equal magnitude moment vectors orient themselves randomly throughout the sample volume as shown in Fig. 1-3a. Through vector addition the individual moments have a cancellation effect resulting in no net magnetisation [2] of the sample.

#### **1.31 Magnetic moments in a stationary magnetic field $B_0$**

If the sample volume is placed in a static magnetic field with a non-zero component in the z direction the magnetic moment vectors of the protons will align with the field in either a parallel or anti-parallel orientation. Although the magnetic moment



vectors will align in both parallel and anti-parallel positions, a greater number will align in the parallel direction giving rise to a net magnetisation of the sample as shown by the big vector arrow of Fig. 1-3 b. The equations of motion for these moment vectors can be written by equating the rate of change in angular momentum  $\mathbf{I}$  to the torque between the magnetic moment and the magnetic field  $\mathbf{B}$ . The equation of motion becomes:

$$\hbar d\mathbf{I}/dt = \boldsymbol{\mu} \times \mathbf{B} \quad (1-11)$$

However revisiting Eq. 1-1, we may eliminate  $I$  to get:

$$d\boldsymbol{\mu}/dt = \gamma \boldsymbol{\mu} \times \mathbf{B} \quad (1-12)$$

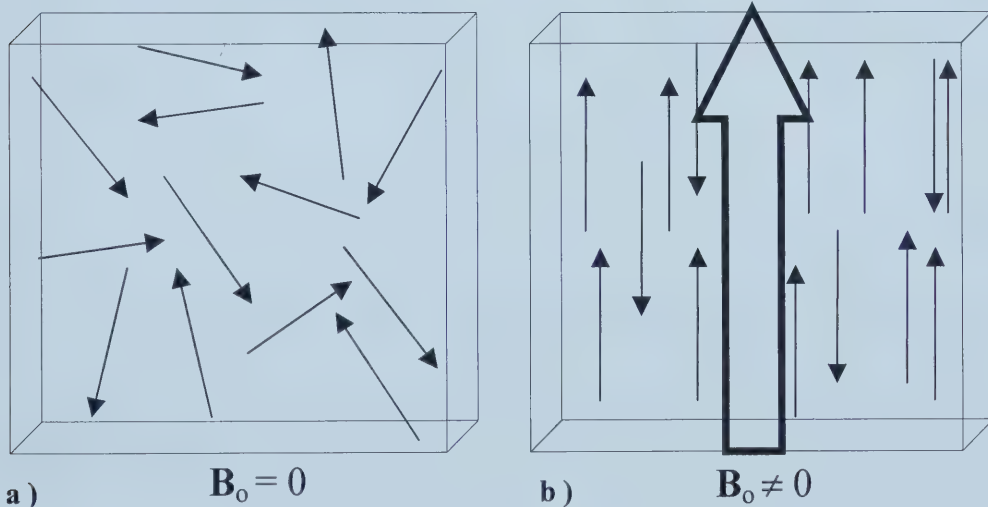


**Figure 1-3**

*An ensemble of individual magnetic moment vectors is shown. In (a) they are arranged in random direction due to the absence of a magnetic field, thus with subsequent zero net magnetization of the volume. In (b) they are aligned both parallel and anti parallel with respect to the non zero  $B_0$  field resulting in a net magnetisation of  $M_0$  represented by the large arrow.*



If  $\mathbf{B}$  is a static field in the z direction of magnitude  $\mathbf{B} = (0,0,B_0)$ , then we can solve the equations of motion for the different components of  $\mu$  which are [2]:

$$d\mu_x/dt = \gamma\mu_y B_0 \quad (1-13a)$$

$$d\mu_y/dt = -\gamma\mu_x B_0 \quad (1-13b)$$

$$d\mu_z/dt = 0 \quad (1-13c)$$

Solving these first order differential equations give the solutions:

$$\mu_x(t) = \mu_{x0} \cos \omega_0 t - \mu_{y0} \sin \omega_0 t \quad (1-14a)$$

$$\mu_y(t) = \mu_{x0} \sin \omega_0 t + \mu_{y0} \cos \omega_0 t \quad (1-14b)$$

$$\mu_z(t) = \mu_{z0} \quad (1-14c)$$

where  $\omega_0 = -\gamma B_0$  and thus the magnetic moments precess in a negative sense about the Z axis and with a frequency which is proportional to the magnetic field in which it resides. It is worthwhile to bring to the readers' attention that this is the same value derived in Eq. 1-7.





In a state of thermal equilibrium  $\mu$  will have a random transverse phase throughout the sample resulting in no net transverse plane magnetisation due to vector cancellation. In the z direction the magnetisation will be determined through addition of the Z components as described by Eq. 1-10.

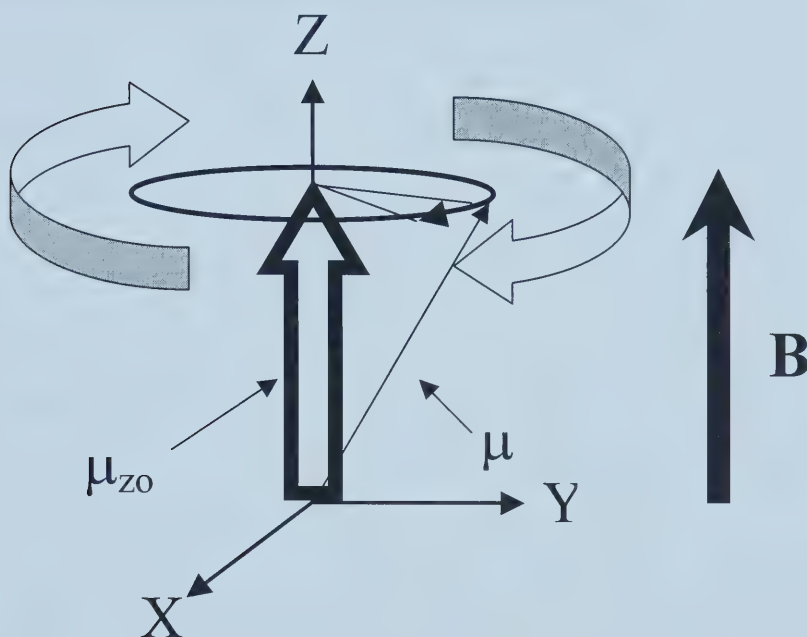


Figure 1-3

Shows the magnetic moment vector of a proton in a static magnetic field  $B$  orientated in the Z direction of the Cartesian co-ordinate system. Notice that  $\mu$  precesses about the Z axis in a negative sense.



### **1.32 Magnetic moments in a stationary magnetic field and a radiofrequency (RF) circularly polarized magnetic field $B_1(t)$**

Excitation of the NMR spin system is done through the application of a circularly polarized magnetic field applied by a pulse called an RF pulse. If a circularly polarized magnetic field of magnitude  $B_1$  (RF pulse) is applied in a direction orthogonal to the static magnetic field  $B_0$ , the total  $B$  becomes:

$$\mathbf{B} = \mathbf{B}_0 + \mathbf{B}_1(t) \quad (1-16)$$

where:

$$\mathbf{B}_0 = (0, 0, B_0) \quad (1-17)$$

and:

$$\mathbf{B}_1 = (B_1 \cos \omega t, -B_1 \sin \omega t, 0) \quad (1-18)$$

which results in:

$$\mathbf{B} = (B_1 \cos \omega t, -B_1 \sin \omega t, B_0) \quad (1-19)$$



The motion of  $\mu$  becomes considerably more complex during excitation when dealing with both a static magnetic field and a circularly polarized magnetic field. In order to make the process more intuitive, we shall change our reference frame from the basic Cartesian laboratory frame, in which we have been working thus far, to a rotating reference frame [5]. The rotating reference frame can be likened to standing on a merry-go-round, versus the laboratory frame, which can be likened to standing beside a merry-go-round. If standing on the ground beside a merry-go-round, the motion of the merry-go-round's model horses will appear sinusoidal moving in three dimensions. If however, you were to stand on the merry-go-round, the apparent motion of the horses would break down into only up and down components, a much less complex motion.

The rotating reference frame rotates in the same sense with the same frequency as the applied  $\mathbf{B}_1(t)$  in Fig. 1-4. The components of the magnetic moment vectors in the rotating reference frame denoted by subscript  $\rho$  are related to the components in the lab frame through the equations:

$$\mu_{x\rho} = \mu_x \cos\omega t + \mu_y \sin\omega t \quad (1-20 \text{ a})$$

$$\mu_{y\rho} = -\mu_x \sin\omega t + \mu_y \cos\omega t \quad (1-20 \text{ b})$$

$$\mu_{z\rho} = \mu_z \quad (1-20 \text{ c})$$

where  $\omega$  is the frequency of the applied  $\mathbf{B}_1$  field.



By applying the new  $\mathbf{B}$  of Eq. 1-19, to the equation of motion in Eq. 1-12 and then converting the equations from the lab reference frame to the rotating reference frame, we get the following differential equations:

$$d \mu_{xp} / dt = (\gamma B_0 + \omega) \mu_{yp} \quad (1-21 \text{ a})$$

$$d \mu_{yp} / dt = -(\gamma B_0 + \omega) \mu_{xp} + \gamma B_1 \mu_{zp} \quad (1-21 \text{ b})$$

$$d \mu_{zp} / dt = -\gamma B_1 \mu_y \quad (1-21 \text{ c})$$

These equations can be combined in a more simple form:

$$d \mu_p / dt = \gamma \mu_p \times \mathbf{B}_{\text{eff}} \quad (1-22)$$

where

$$\mathbf{B}_{\text{eff}} = B_{1xp} \hat{i}_p + (B_0 + \omega/\gamma) \hat{k}_p \quad (1-23)$$

This result is of the same form that appears in Eq. 1-12, which is the equation for the laboratory reference frame. The primary difference between the two equations is the  $\mathbf{B}_{\text{eff}}$  term, which appears in Eq. 1-22 and has components in both the X and the Z directions. Thus, in the rotating reference frame, the magnetic moment will precess in a cone about the  $\mathbf{B}_{\text{eff}}$  axis at a frequency of  $\omega = \gamma B_{\text{eff}}$ .





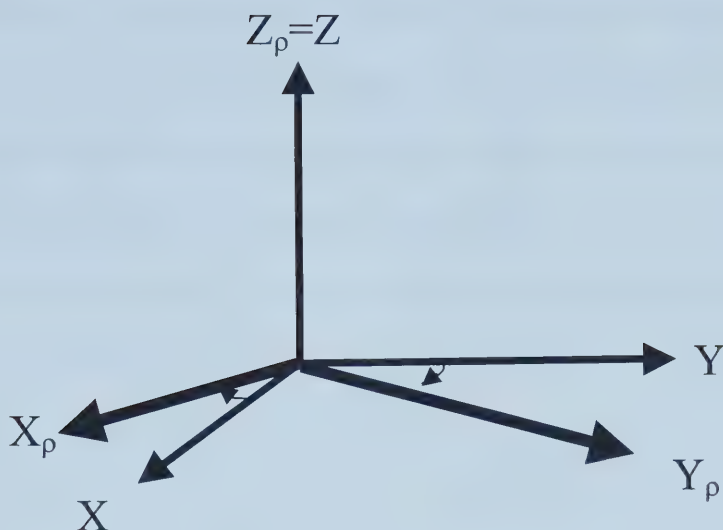


Figure 1-4

Shows the rotating frame of reference ( $X_\rho$ ,  $Y_\rho$ ,  $Z_\rho$ ) with respect to the laboratory frame of reference ( $X$ ,  $Y$ ,  $Z$ ). The rotating frame precesses at the same frequency and in the sense as  $\mathbf{B}_1(t)$ .

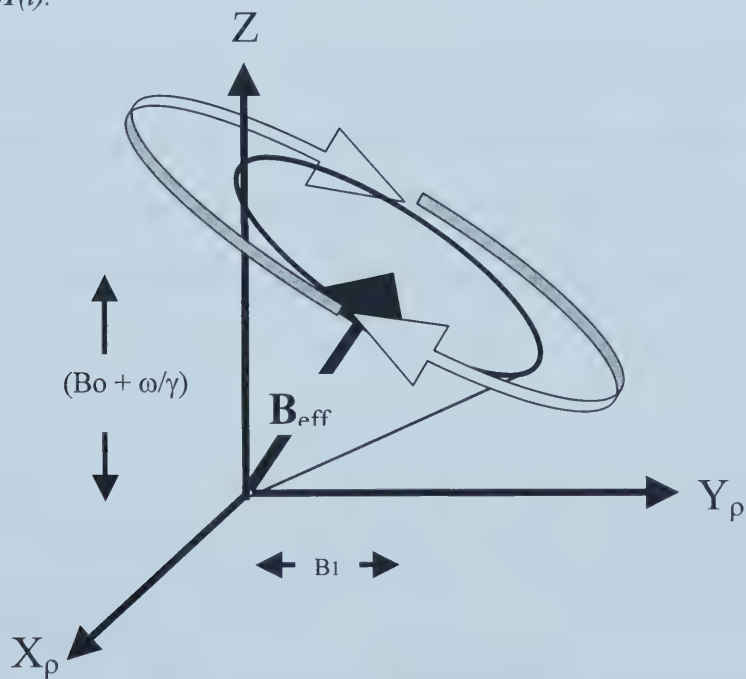


Figure 1-5

The motion of the magnetization vector in the rotating frame of reference is shown.



When  $\omega$  is applied such that  $\omega = -\gamma B_0$ ,  $\mathbf{B}_{\text{eff}}$  becomes parallel to  $\mathbf{B}_1$ . In the case where  $\mathbf{B}_1$  is applied at the Larmor frequency along the  $Y_p$  direction, the magnetization vector will precess about  $Y_p$  in the XZ plane. Thus by applying a circularly polarized magnetic field  $B_1$  for a time  $t$ , the classical magnetic moment of the protons can be tipped from the  $z$  axis into transverse plane giving rise to a detectable signal [4]. The angle away from the  $Z$  direction that a given pulse rotates the magnetic moment vector is referred to as the flip angle. The flip angle for an on-resonant RF pulse is defined by

$$\alpha(t) = \gamma \int B_1(t) dt \quad (1-24)$$

After being tipped, the magnetic moment may have components in both the  $Z$  direction and the  $XY$  plane. Components in the  $Z$  direction are referred to as longitudinal magnetization and are given by the value  $M_z$ . Components in the  $XY$  plane are referred to as the transverse magnetization and given the complex value of  $M_{xy}$  defined by:

$$M_{xy} = M_x + iM_y \quad (1-25)$$

where  $i$  is the square root of  $-1$ .



A  $90^\circ$  on-resonant pulse is shown in Fig. 1-6 from the perspective of both the rotating and laboratory frame of reference. From this example, it is easy to see the simplification of motion which results from observing within the rotating frame of reference. This process of tipping the magnetic moment into the XY plane is referred to as excitation and is the process by which the NMR signal is generated.

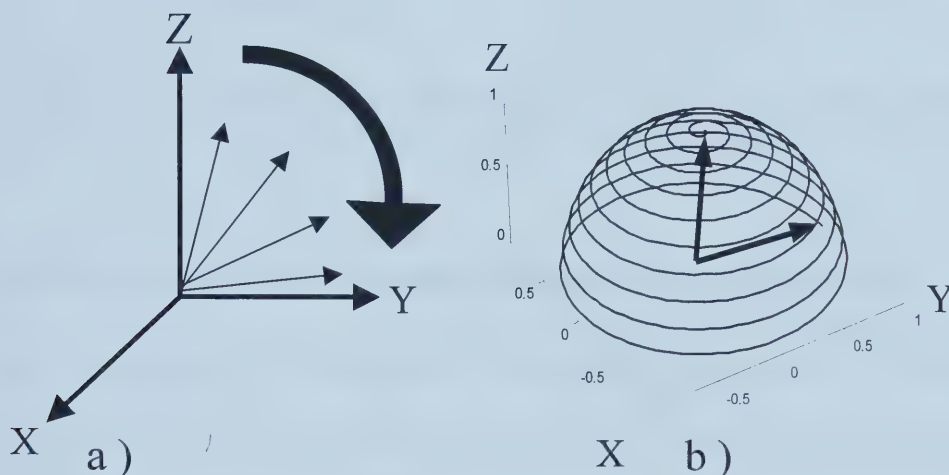


*Figure 1-6*

*The classical magnetization vector during a  $90^\circ$  excitation is viewed from both the rotating reference frame in (a) and the laboratory reference frame in (b).*

After the magnetic moment has been flipped into the transverse plane, the excitation pulse  $B_1$  is turned off. At this point the situation returns to the one described in Section 1.3.1 in which the transverse magnetization precesses about the Z axis at the frequency of  $\omega_0$ . This precession of the magnetic moment about the Z axis will induce a current in a conductor placed adjacent to the sample [5]. If we perform a Fourier transform on this signal we get a sharp peak at the resonant frequency of the magnetic moment as shown in Fig. 1-7.



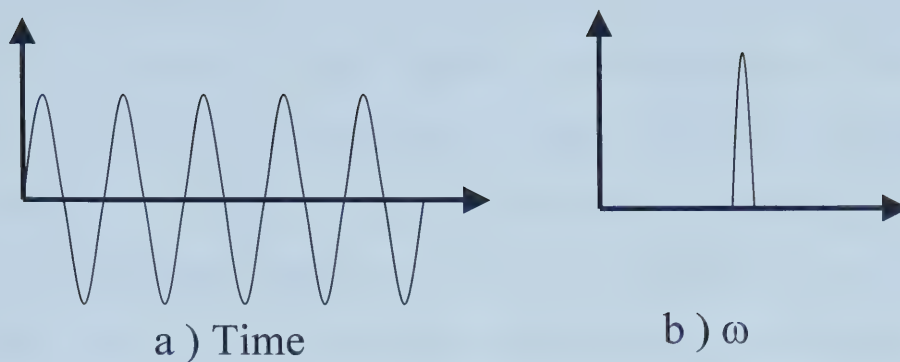


Figure 1-7

*The time-dependent emf signal resulting from the precession of the magnetic moment about the z axis is shown in (a) and the resulting power spectrum in (b).*

## 1.4 Relaxation mechanisms as contrast mechanisms and the Bloch equations

After excitation, magnetic moments begin to relax to their steady state values, which results in the decay of the measurable time domain NMR signal and the regrowth of the steady-state longitudinal equilibrium magnetization. These relaxation processes are governed by two related processes: longitudinal and transverse relaxation.

### 1.41 Longitudinal Relaxation

Longitudinal relaxation is characterized by a relaxation time  $T_1$ . It involves the change of the  $M_z$  component of the magnetization moment from the excited state to that of the thermal equilibrium state  $\mathbf{M}_0$ .  $T_1$  relaxation is governed by the energy exchange rate between resonant nuclei and the surrounding molecular lattice. Energy is exchanged through randomly changing magnetic fields resulting from motion of





the surrounding dipole lattice. Because different materials have different molecular lattices, the energy exchange rates are also different. Because of the greater energy required for relaxation at higher frequencies, longitudinal relaxation occurs at a slower rate at higher  $B_0$  fields as shown in Table 1. Independent observations by Bloch [6] and Purcell [7] showed that the T1 relaxation rate was related to the degree by which the magnetic moments have been removed from the thermal equilibrium  $M_0$  state. The change in the longitudinal component can be described by the equation:

$$dM_z(t)/dt = 1/T1(M_0 - M_z(t)) \quad (1-26)$$

where  $M_0$  is the initial thermal equilibrium state of the magnetization and T1 is constant for various tissues describing the molecular interaction rate. Solving this first order differential equation gives:

$$M_z(t) = M_0 + (M_z(0) - M_0)e^{-t/T1} \quad (1-27)$$

Thus for a 90° pulse the equation becomes:

$$M_z(t) = M_0(1 - e^{-t/T1}) \quad (1-28)$$

and for a 180 deg pulse the equation becomes:



$$M_z(t) = M_0(1 - 2e^{-t/T_1}) \quad (1-29)$$

Note that the quickest longitudinal relaxation comes immediately after being excited and the further the moment is away from the equilibrium state the quicker it relaxes. Table 1 illustrates the differences in T1 times for different tissues [8]. Discrimination between tissues can then be obtained through the appropriate choice of timings and imaging experiments to highlight the tissues of interest.

<b>Tissue</b>	<b>T1(ms) @ 1.5 Tesla</b>	<b>T1(ms) @ 3.0 Tesla</b>
<b>White Matter</b>	790	850
<b>Grey Matter</b>	920	1300
<b>Cerebrospinal Fluid</b>	4316	4316
<b>Muscle</b>	870	1073
<b>Fat</b>	250	419

*Table 1-1*

*T1 times for various tissues at  $B_0$  Field strengths of 1.5 and 3.0 Tesla at the temperature of 37 deg Celsius.*



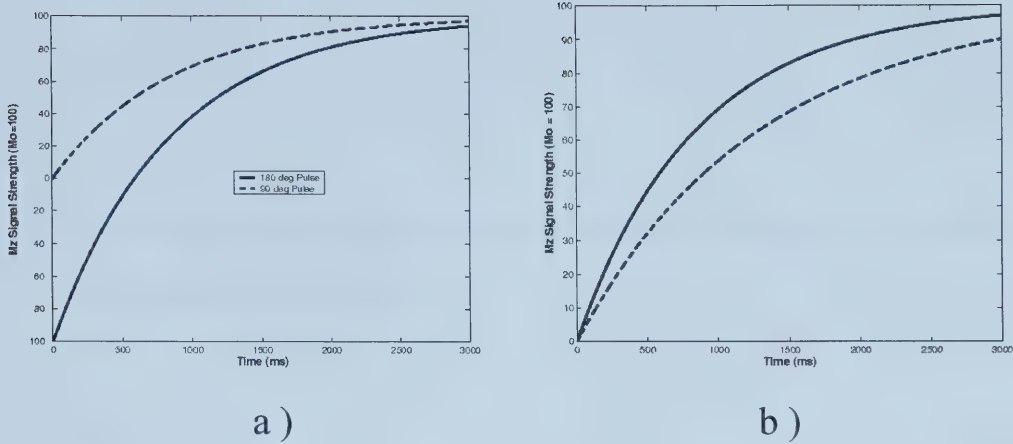


Figure 1-8

(a) Shows relaxation of white matter ( $T_1 = 850\text{ms}$ ) having undergone a 90 degree and a 180 degree RF pulse. (b) Shows the relaxation of both white and grey ( $T_1 = 1300\text{ms}$ ) matter having undergone a 90 deg RF pulse.

#### 1.42 Transverse Relaxation

$T_2^*$  relaxation describes the decay of transverse magnetization through both reversible and non-reversible processes. The equation describing the decay of signal resulting from  $T_2$  relaxation is given by [8]:

$$dM_{xy}(t)dt = -M_{xy}(t)/T_2^* \quad (1-30)$$

where  $M_{xy}$  is the magnetization in the XY plane and  $T_2^*$  is a constant, which describes the transverse relaxation rate. Solving this first order differential equation gives:



$$M_z(t) = M_{xy}(0)e^{-t/T2^*} \quad (1-31)$$

which is the time dependant signal decay after the initial excitation.  $T2^*$  is made up of two components [2] such that:

$$1/T2^*=1/T2+1/T2' \quad (1-32)$$

The component  $T2$  is the result of several factors [9]. One factor is the spin–spin interaction in which an excited dipole produces an on-resonant, perpendicular magnetic field  $\mathbf{B}_1$  which excites surrounding dipole moments. Another factor is molecular rotations and vibrations causing  $\omega_0$  to fluctuate, resulting in a loss of coherent signal shown in Fig. 1-9. The  $T2$  component of  $T2^*$  is irreversible resulting ultimately in a complete loss of coherent signal. For a given magnetic field of 1.5T, average  $T2$  times are shown in Table 2 [8]. The component of  $T2'$  arises from the fact that protons never experience a purely homogenous static magnetic field. Inhomogeneity in the  $\mathbf{B}_0$  field can arise from surrounding sources of magnetism in the sample or from imperfections in the manufacturing of the magnet. Another factor is different susceptibilities within a sample.





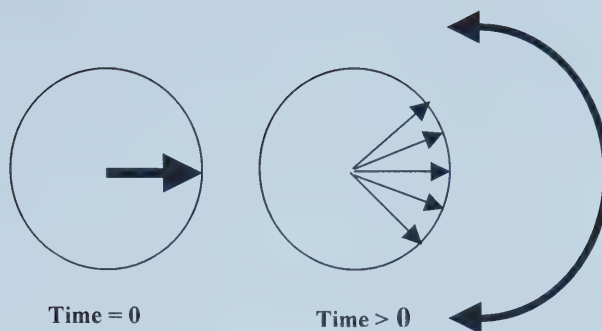


Figure 1-9

Fluctuating  $\omega_0$  can result in a spread of phase and subsequent loss of coherent signal.

Tissue	T2
White Matter	92
Grey Matter	100
Muscle	470

Table 1-2

The average T2 times are shown for brain constituents at 1.5 Tesla.

## 1.5 Spatial Encoding

Spatial encoding is the process of encoding the location of signal within the NMR experiment. For our purposes, the final product of spatial encoding will be an image that relates signal to spatial location. Spatial encoding involves the addition of a



linearly varying magnetic field of slope  $G$  to the existing bulk field  $\mathbf{B}_0$ . Thus the magnetic field along the direction of the gradient field becomes:

$$\mathbf{B}_{\text{total}} = \mathbf{B}_0 + \mathbf{G}_d \bullet \mathbf{d} \quad (1-33)$$

where  $d$  is the displacement along the direction of the gradient  $G_d$ . Substituting this into Eq. 1-7 gives us the resultant linearly varying resonant frequency:

$$\omega_{\text{total}} = \gamma(\mathbf{B}_0 + \mathbf{G}_d \bullet \mathbf{d}) \quad (1-34)$$

and in the rotating frame of reference this equation simplifies to:

$$\omega_p = \omega(d) = \gamma \mathbf{G}_d \bullet \mathbf{d} \quad (1-35)$$

This result is used in three ways to encode and image which will be described in the following sections.

### **1.51 Slice Selection.**

In slice selection, a gradient  $\mathbf{G}_z$  is applied simultaneously with a RF pulse of set bandwidth ( $BW_{rf}$ ) at frequency  $\omega_{rf}$ . The gradient has the effect of spreading out the Larmor frequencies across the direction of the gradient. The RF pulse will excite those spins which have Larmor frequencies within the bandwidth of the pulse [10].



The slice thickness can be thus controlled by adjusting the strength of the gradient such that:

$$\text{Slice Thickness} = BW_{\text{rf}}/G_z \quad (1-36)$$

where  $BW_{\text{rf}}$  is the bandwidth of the RF pulse and  $G_z$  is the gradient strength in the slice direction. It is also possible to move the location of the slice by adjusting centre frequency at which the RF pulse is applied.

### 1.52 Frequency encoding

Frequency encoding is accomplished by applying a magnetic gradient  $G_x$  during signal acquisition. This gradient causes a spreading in the Larmor frequencies of the acquired signal. When Fourier transformed the signal is separated into its frequency components, which are related to its spatial positions. The bandwidth BW of the received signal is described in the equation:

$$BW_{\text{freq}} = \gamma G_x \text{FOV}_x \quad (1-37)$$

where  $G_x$  is the frequency encoding gradient strength and  $\text{FOV}_x$  is the field-of-view in the frequency encode direction and is equal to  $x_{\text{max}} - x_{\text{min}}$ . Provided that the object does not extend beyond  $\text{FOV}_x$  aliasing is avoided by satisfying the Nyquist criteria:



$$\text{Sampling Rate} \geq 2\gamma G_x x_{\max} \quad (1-38)$$

However, typically the data acquisition system will apply an analogue filter to remove any frequencies above or below the range of interest. Thus aliasing is not a concern in the frequency direction.

Spatial resolution in the frequency direction is given by the equation:

$$\text{Pixel Size} = \Delta x = \text{FOV}_x / N_{\text{freq}} \quad (1-39)$$

where  $N_{\text{freq}}$  is the number of points taken in the frequency encode direction.

### **1.53 Phase Encoding**

Phase encoding is similar to frequency encoding in that a type of pseudo frequency is developed through incrementing the phase through repeated acquisitions. We shall call the phase encoding direction the Y direction. To encode a phase increment, a gradient  $G_y$  is applied in the desired direction for a time  $t_y$ . During this period the Larmor frequencies spread according to the physical offset from the gradient center.

After  $t_y$ , the gradient is then turned off resulting in a return to the Larmor frequency and a linear phase distribution in the Y direction (see Fig. 1-10). The phase acquired over this period is described by:





$$\Theta = \gamma \int_{t_y} (G_y(t) \bullet y) dt \quad (1-40)$$

where  $G_y$  is the gradient in the phase or Y direction and  $t_y$  is the duration of the phase gradient. Between each line of acquisition, the phase encode gradient is incremented in discrete linear steps of  $G_{yinc}$  resulting in a linear distribution of pseudo frequencies that are directly proportional to the spins Y offset. To avoid aliasing, the increment in the phase encode direction is chosen such that there is a  $2\pi$  ( $\pm\pi$ ) phase shift across the sample thus:

$$2\pi = \gamma \int_{t_y} (G_{yinc}(t) \bullet FOVy) dt \quad (1-41)$$

where  $FOV_y$  is the field-of-view in the Y direction. Spatial resolution in the phase direction is given by the equation:

$$\Delta y = FOV_y / N_{pe} \quad (1-42)$$

where  $N_{pe}$  is the number of phase encodes steps in the Y direction.



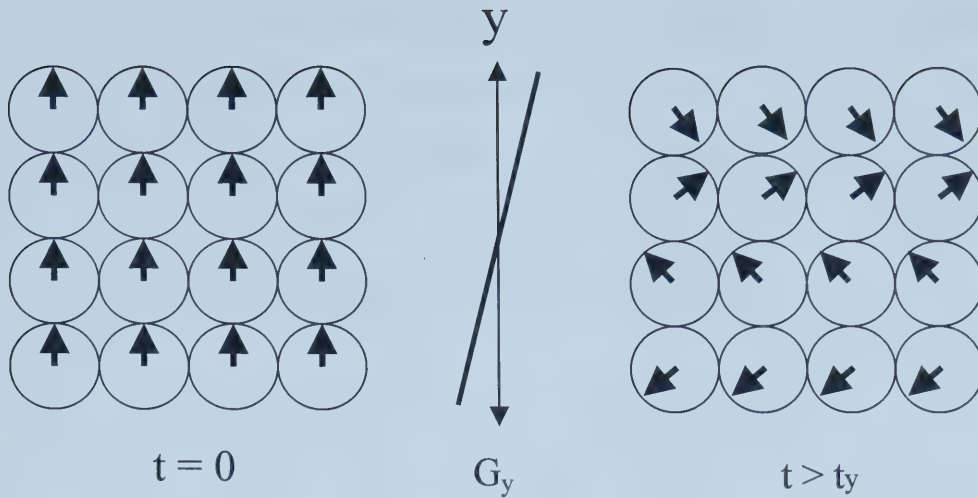


Figure 1-10

At left is the initial phase distribution following tipping into the transverse plane. At right is the resultant phase distribution after the application of the phase gradient  $G_y$  for time  $t_y$ .

#### 1.54 Radio frequency (RF) excitation pulses

The RF pulse is applied at a specific frequency called the transmission frequency and its amplitude is modulated in the time domain. If the time domain pulse envelope is Fourier transformed, the frequency response of the RF pulse is the result. In slice selection, when the slice select gradient is applied this frequency response profile becomes the excitation profile or slice profile. In Eq. 1-36 the term  $BW_{rf}$  refers to the full width of the frequency response at half the maximum value of the frequency response as shown in Fig. 1-11.



Two of the primary pulses used in NMR are termed hard and soft. The hard pulse, Fig. 1-12a, has a square time domain profile and the frequency response of Fig. 1-12b is a sinc function. The benefit of this pulse is that it can generate tip angles with very short time frames. The pulse has a broadband frequency response as compared to other pulses, which gives it a poor slice profile as compared to other pulses.

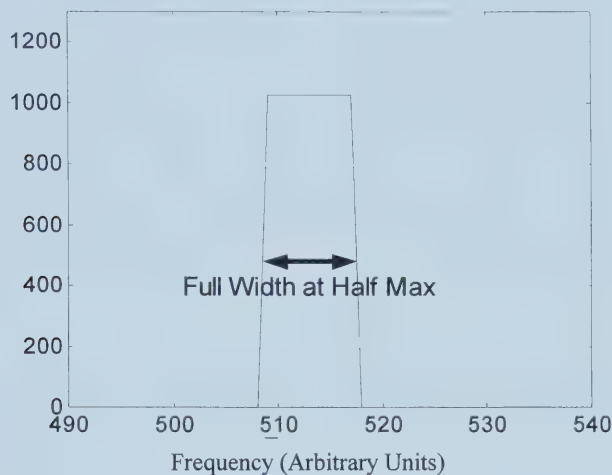


*Figure 1-11*

*The Bandwidth for a given RF pulse is defined as the full bandwidth at half the maximum amplitude of the frequency response.*

A soft pulse shown in Fig. 12c, in this case a truncated sinc pulse, has a long duration play out but gives a narrow, rectangular band frequency response shown in Fig. 12d [11]. This narrow, sharp frequency response is desirable in imaging to give a well-defined slice. For any pulse, the time domain and frequency response are inversely proportional thus long pulses have narrow bandwidths and short pulses have broad bandwidths. To stay within power constraints imposed by RF power amplifiers a compromise must be made between profiles in the time and frequency domains.



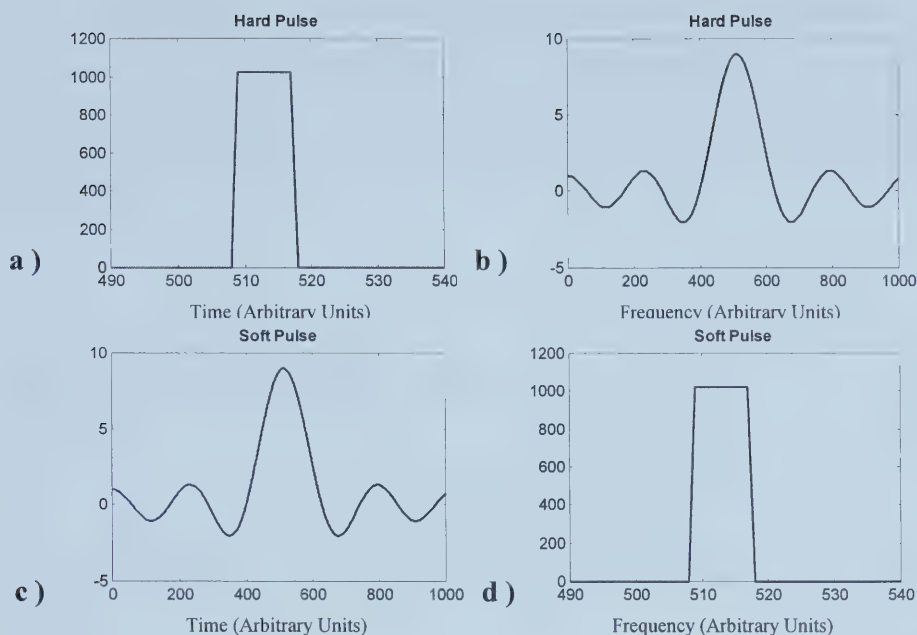


*Figure 1-12*

*Relative time and frequency relations are shown for a hard pulse (a,b) and a soft (sinc) pulse (c,d).*

## 1.6 The Signal Equation and K space

In the last sections we have talked about the creation of signal through the use of RF pulses and the spatial encoding of signal through the use of magnetic gradients. We shall now look at the resultant signal received and how this signal is used in the creation of an image. In order to keep things as simple as possible, we shall look at a two dimensional sequence which has been demodulated by  $\omega_0$  using a phase sensitive detector. Furthermore we shall also ignore the T2 relaxation term in Eq. 1-31.





The receiver coil detects signal from all precessing spins within the sample. This is localized to a region of interest by the use of the previously described slice selection. The sum of all the received signal from  $M(x,y)$  within this region of interest can be written as the integral:

$$S(t) = \int_x \int_y M(x,y) e^{-i2\pi[k_x(t)x + k_y(t)y]} dx dy \quad (1-43)$$

where  $k_x$  and  $k_y$  are the time integrals of the gradient waveforms in the x and y directions:

$$k_x = \gamma \int_0^t G_x(t) dt \quad (1-44a)$$

$$k_y = \gamma \int_0^t G_y(t) dt \quad (1-44 b)$$

Note that Eq. 1-43 has the form of a Fourier transform [12].

The terms  $k_x$  and  $k_y$  are positions in k-space. K-space is a space in which frequency and phase take the place of displacement in real space. The k-space data of an image has as many points as the real image has voxels thus in order to acquire a complete, high-resolution image, all k-space points must be sampled. As described in Eqs. No 1-43a,b k-space is traversed by the application of gradients. We shall now look at how a single acquisition of a 2D gradient echo sequence samples k-space.



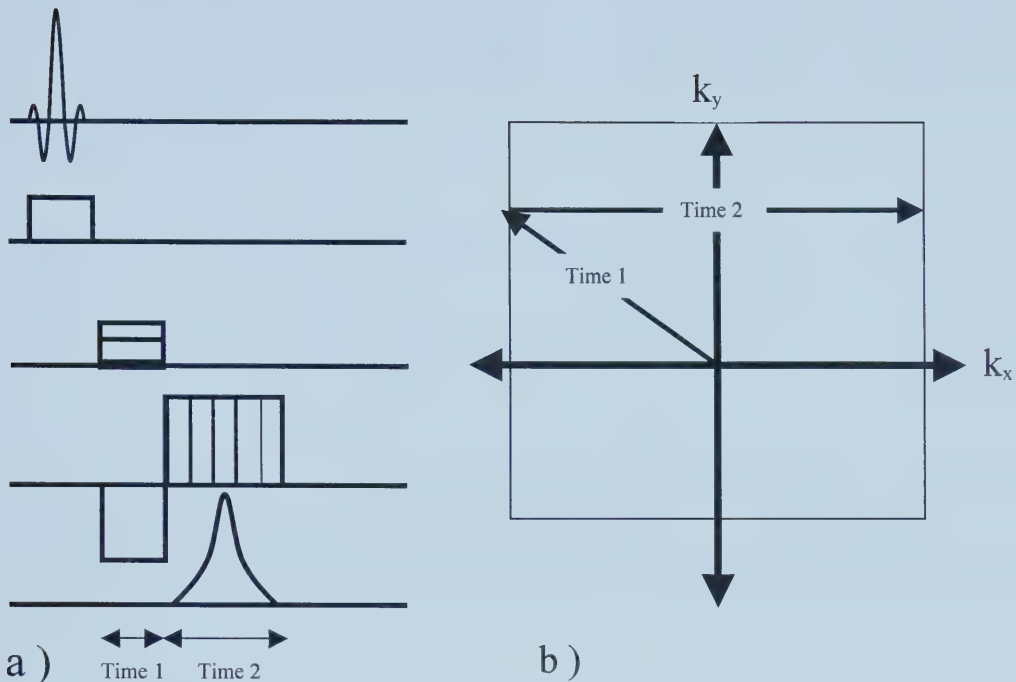


*Figure 1-13*

*At left in (a) is a typical 2D gradient echo pulse sequence. At right is the k-space traversal pattern caused by the application of gradients. See text for details.*

During time 1 of the sequence in Fig. 1-13a, both the phase encode and the read encode gradients are on which results in a shift in k-space coordinates as shown in Fig. 1-13b. During time 2 of the sequence in Fig. 1-13a, the frequency encode gradient is turned on and data is acquired Fig. 1-13b. The result is that an entire  $k_x$  row of k-space is sampled [8]. During the next acquisition everything repeats exactly except the height of the phase encode gradient ( $G_y$ ) which is incremented in order to allow a new  $k_y$  line of k-space to be sampled. Thus by incrementing the  $G_y$  by  $G_{yinc}$



through repetitions of the experiment it is possible to sample all of k-space. K-space may be sampled in several different manners and is generally optimized for each application [2,13-16]. In k-space, the field of view is related to the sampling rate through the equations:

$$FOV_x = 1/\Delta k_x = (2\pi N_{read}/\gamma G_x \text{Time}_2) = \text{Sampling rate in } k_x \quad (1-45a)$$

$$FOV_y = 1/\Delta k_y = (2\pi / \gamma G_{yinc} \text{Time}_1) = \text{Sampling rate in } k_y \quad (1-45b)$$

Note that these equations are essentially the same as Eqs. 1-37 and 1-41. Thus spatial resolution in the object domain can be equated to the frequency domain through the equations [8]:

$$\Delta x = FOV_x / N_{read} = 1/\Delta k_y N_{read} \quad (1-46a)$$

$$\Delta y = FOV_y / N_{pe} = 1/\Delta k_y N_{pe} \quad (1-46b)$$

and pixel size is hence inversely proportional to the number of frequency or phase encodes.



## 1.7 Other Methods of Tissue Contrast

### 1.71 Fat Suppression

Water exists as two hydrogen atoms bound to one oxygen atom whereas fat exists as a large number of hydrogen atoms bound to a long carbon atom spine. This difference in molecular environment results in a corresponding difference in magnetic environment. As a result of this difference in local field, the Larmor frequency of the hydrogen nuclei in fat will be offset from those of water. In general this shift in Larmor frequency experienced by any hydrogen nuclei bond in a different magnetic environment is called a chemical shift. In fat this shift is ~3.5 ppm (see Fig. 1-11). The ppm scale is a field independent scalar [9], which is defined by:

$$\omega_{\text{ppm}} = \frac{(\omega_i - \omega_{\text{ref}})}{\omega_{\text{ref}}} * 10^6 \quad (1-47)$$

where  $\omega_i$  is the resonant frequency of interest and  $\omega_{\text{ref}}$  is the frequency that the frequency is being referenced to.

This offset in Larmor frequency as compared to the water peak gives rise to a physical displacement of the fat in an image. This phenomenon also allows us to selectively excite one peak while leaving the other unaffected. This is commonly used to saturate fat by selectively exciting the fat peak and then spoiling the signal





with the magnetic gradients before using the spatially selective imaging pulse. It is also possible to suppress fat by altering the echo time so that water and fat are  $180^\circ$  out of phase.

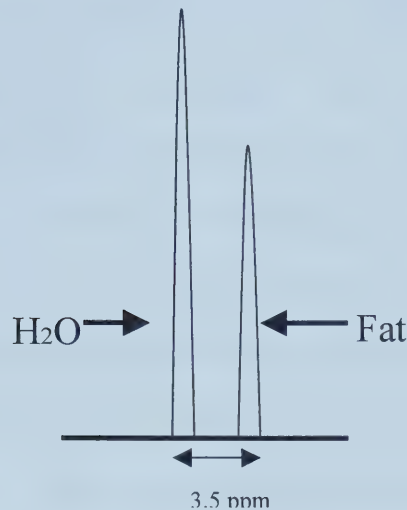


*Figure 1-14*

*As illustrated, in the power spectrum the resonant frequencies of water and fat are separated by 3.5ppm or 440 Hz @ 3.0 Tesla.*

## **1.72 Magnetization Transfer (MT)**

Water molecules that exist in tissues can be divided into the two categories of those that are freely moving and those that are bound having been absorbed by macromolecules such as fats, proteins etc. Hydrogen protons from the bound water molecules ( $H_b$ ) have extremely short  $T_2$  constants  $< 10\text{msec}$  because they rapidly dephase after having been excited into the transverse plane. This short  $T_2$  gives  $H_b$  a large bandwidth power spectrum, centred on the water peak. The wide bandwidth enables off-resonant excitation of  $H_b$  species while having minimal effect on freely



moving protons ( $H_f$ ) [9]. (See Fig. 1-15). Any effect that does incur from the off resonant pulse itself is termed the direct effect. These short  $T_2$   $H_b$  protons contribute little signal to an image; however when irradiated, the  $H_b$  protons exchange magnetization with the  $H_f$  protons decreasing the steady state magnetization of the  $H_f$  protons. This exchange of magnetization between the two pools is termed magnetization transfer and provides another contrast mechanism in imaging. The primary mechanism for this exchange is through space via dipolar coupling. Dipolar coupling results when a proton is close enough to another proton such that its magnetic field affects the other proton thus inducing mutual transitions of spin states in both protons. Thus irradiated,  $H_b$  protons will equilibrate with  $H_f$  protons resulting in the decrease in the steady state longitudinal magnetization of the  $H_f$  protons. Magnetization transfer is usually accomplished by constant wave (CW) [17] irradiation or by Pulsed magnetization transfer. In CW MT, a long off-resonant hard pulse is played out before an on-resonant excitation pulse is used to sample  $H_f$  signal. In pulsed MT, short duration off resonant soft pulses are used to incur MT before sampling the  $H_f$  signal with an on resonant excitation pulse. Pulsed MT is generally the method of choice in imaging application due to the ease of which can be fit into an imaging pulse sequence without requiring excessive time.



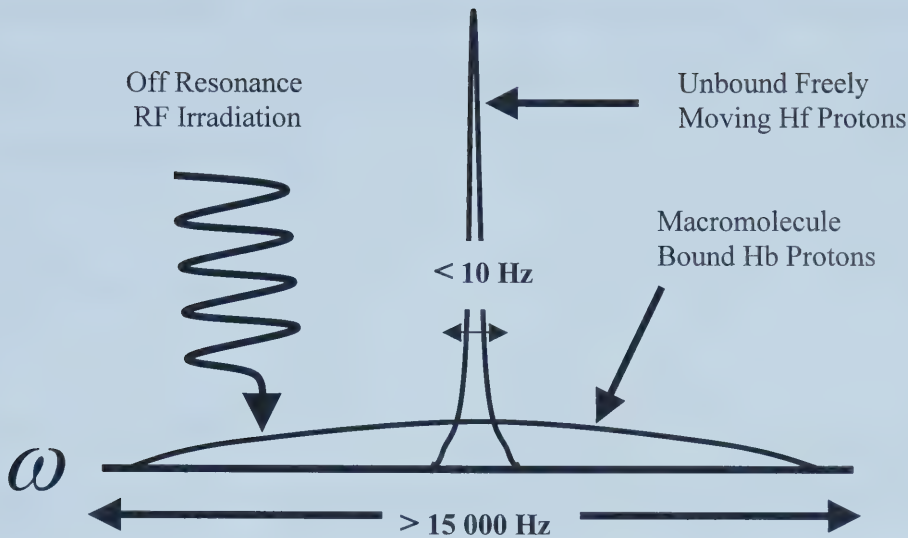


Figure 1-15

*The power spectrum for bound Hb is much more broad than for freely moving Hf protons allowing excitation by off resonance RF irradiation.*

### 1.8 Power Deposition and the Specific Absorption Rate (SAR)

It is important to keep in mind that the RF energy used in NMR can be deposited in the body as heat. The power deposited in a sphere from a circularly polarized magnetic field can be determined using Faraday's law of electromagnetic induction [18] and is given by:

$$P = 2/15(\pi\sigma\omega^2 B_1^2 R^5) \quad (1-48)$$



where  $\sigma$  is the conductivity of the sphere,  $R$  is the radius of the sphere and  $\omega$  is the transmission frequency of the circularly polarized magnetic field. If the experiment is being performed with pulses that are on resonance, we can substitute  $\omega$  with  $\gamma B_0$  giving the equation below [2]:

$$P = 2/15(\pi\sigma\gamma^2 B_0 B_1^2 R^5) \quad (1-49)$$

Note that the power deposited is related to the square of both the strength of the applied  $B_1$  and the bulk magnetic field  $B_0$ . Thus power deposition in RF intensive sequences becomes a matter of concern as one moves to higher magnetic fields. For example, for the same flip angle and RF pulse shape, the power deposition will be 4 times greater at 3.0 T than it is at 1.5 T.

In order to deal with the safety concerns of RF heating guidelines have been set up by the Federal Drug Administration (FDA) to ensure patient safety. These guidelines have been designed around what is called Specific Absorption Rate (SAR). SAR is defined as:

$$SAR = P/M \quad (1-50)$$





where  $M$  is the mass of the tissue being irradiated. In the head FDA regulations require maximum SAR limit of  $3\text{W/kg}$  over 9 minutes with a maximum short duration SAR of  $9\text{W/kg}$  over any 10 second period [19].



## 1.9 References:

1. Potchen, E., *et al.*, *Magnetic Resonance Angiography: Concepts and Applications*. 1993, St. Louis: Mosby.
2. Haacke, E.M., *Magnetic Resonance Imaging, physical principles and sequence design*. 1999: John Willey & Sons.
3. Luiten, A.L., *Fundamentals of NMR imaging*. *Diag. Imag. Clin. Med*, 1984. **53**: p. 4-12.
4. Hinshaw, W.S., *An introduction to NMR imaging*. *Proceeding of the IEEE*, 1983. **71**(3): p. 338-350.
5. Bronskill, M.J., *The physics of MRI 1992 AAPM summer school proceeding*. 1993, Woodbury: American Institute of Physics, Inc.
6. Bloch, F., *Nuclear induction*. *Physical Review*, 1946. **70**: p. 460-474.
7. Purcell, E.M., H.C. Torrey, and Pound, R.B. *Resonance absorption by nuclear magnetic moments in a solid*. *Physical Review*, 1946. **69**: p. 37-38.
8. Nishimura, D.G., *Principles of magnetic resonance imaging*. 1996: Stanford University.
9. Brown, M.A., Semelka, R.C., *MRI Basic Principals and Applications*. 1995: John Wiley & Sons.
10. McRobbie, D.W., *Investigation of slice characteristics in NMR imaging*. *Phys. Med. Biol.*, 1986. **31**(6): p. 613-626.
11. Freeman, R., *Shaped radiofrequency pulses in high resolution NMR*. *J. of Progress in NMR Spectroscopy*, 1998. **32**: p. 59-106.



12. Bracewell, R.N., *The Fourier Transform and its Applications*. 1978: McGraw-Hill. pp. 122.
13. Bishop, J. and Plewes, D. *Stimulated echo effects in fast spin echo images*. in *10th Annual Mtg. Soc. Magn. Reson. in Med*. 1991. San Francisco.
14. Bampton, A.E.H. and Riederer, S.J., *Improved efficiency in magnetization-prepared rapid gradient echo imaging: application to abdominal imaging*. *Magn Reson in Med*, 1992. **25**: p. 195-203.
15. Turner, R., *et al.* *Functional neuroimaging with EPI: sequence issues*. in *Functional MRI of the Brain, A Workshop presented by the SMRM and the SMRI*. 1993. Washington, DC.
16. Wilman, A.H. and Riederer, S.J. *Peformance of an elliptical centric view order for signal enhancement and motion artifact suppression in breath-hold three-dimensional gradient echo imaging*. *Magn Reson Med*, 1997. **38**: p. 793-802.
17. Beaulieu, C. *NMR Study of Water Diffusion and MT in Nerve*. 1995, University of Alberta, PH.D. Thesis.
18. Reitz, J.R., Milford F.J., Christy R.W., *Foundations of Electromagnetic Theory 4<sup>th</sup> edition*.1993: Addison-Wesly
19. Hugg JW, Bernstein MA, Stokar S, Lin C, Rosenfeld D, Felmlee JP, Montag A, Huston JH, Assif B, Reynolds HG. *Routine Clinical Head MRI at 3.0T with Optimized RF Power Management*. In: *Proceedings of the 9th Annual Meeting of ISMRM, Glasgow, Scotland, 2001*. p 1349.



## Chapter 2

### Standard Time-of-Flight MR Angiography

#### 2.1 Introduction

Magnetic resonance angiography (MRA) refers to the imaging of vasculature using MRI. Since the onset of MRA, development has focused on three areas: improving the speed of acquisition, the image resolution and the vessel-to-background contrast. This chapter will focus on the introduction of standard time-of-flight (TOF) MRA.

In 1951 Suryan [1] discovered that flowing water appears to have a shorter  $T_1$  time than stationary water. The reason is that as a slice is repetitively excited with a  $TR < \sim 5 \cdot T_1$ , a partial saturation of  $M_z$  magnetization occurs in the area resulting in a depleted steady state signal. If fresh  $M_z$  enters from outside the region of excitation, it can provide higher signal than that of the existing stationary tissue thus appearing to have a shorter  $T_1$ . It is useful in this case to view  $M_z$  as potential imaging signal from which the transverse magnetization  $M_{xy}$  is sampled. This experiment was later used to look at blood by Singer [2, 3] and much later still by Keller [4] in the form of a two dimensional TOF MRA sequence to image blood vessels.

The basic technique of TOF MRA is shown in Fig. 2-1. To maximize fresh blood inflow, the imaging slab is placed perpendicular to the main direction of blood flow.





To this imaging slab, moderate flip angle excitation pulses are applied with a repetition time substantially shorter than the T1 of the tissues within the imaging volume. The background tissue will see all of the excitation pulses resulting in a substantial depletion of signal. The depleted background signal can be determined from the steady state Bloch equation:

$$M_{xy} = \{M_0[1 - e^{(-TR/T1)}]/[1 - \cos(\alpha)e^{(-TR/T1)}]\} \sin(\alpha) \quad (2-1)$$

where  $M_0$  is the initial longitudinal magnetization, TR is the repetition time defined by the time between successive excitation pulses and  $\alpha$  is the flip angle.

Because blood within the slab is refreshed due to inflow, it will not be subjected to as many RF excitations and thus have a high  $M_z$  relative to the surrounding stationary tissues [5-7]. The signal for blood after receiving the nth RF pulse can be described with the equation:

$$M_{xy}(n) = \{[M_z(n-1) - M_0]e^{(-TR/T1)} + M_0\} \sin(\alpha) \quad (2-2)$$

where  $M_z(n-1)$  is the longitudinal magnetization after the previous RF pulse. The total number n of RF pulses seen by the blood will depend on how fast the blood traverses the volume.



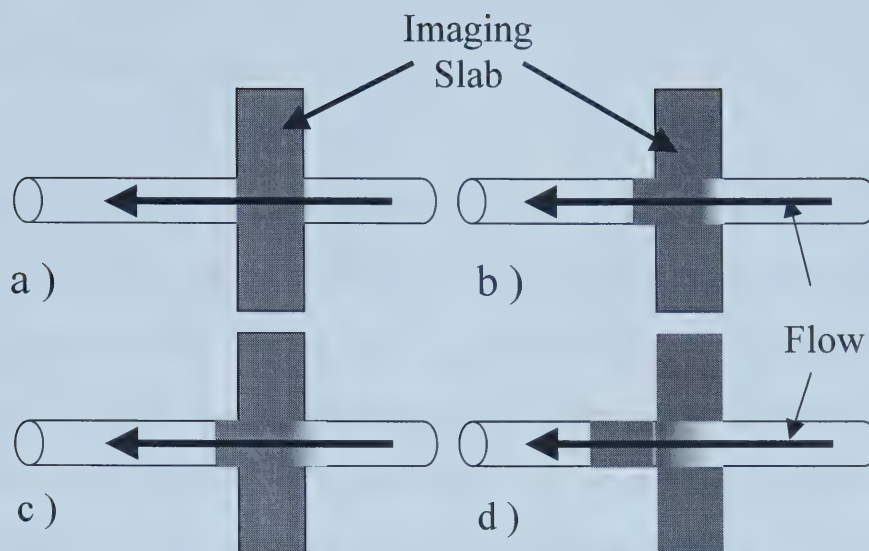


**Figure 2-1**

*In TOF imaging, stationary tissue in the imaged volume sees all RF pulses resulting in a low steady state signal (a-d). Blood flowing into the imaging volume has an undisturbed magnetization resulting in a higher image signal when compared to the stationary tissue b.). As the blood flows through the imaging slab it receives an increasing number of excitation pulses resulting in partially saturated signal near the end of the slab(c,d).*

## **2.2 Two-dimensional vs. Three-dimensional MRA**

Three-dimensional (3D) MRA sequences are preferred over two-dimensional (2D) techniques due to their ability to obtain higher resolution images in the slice select direction, improved signal-to-noise due to increased averaging over the volume, and a shorter TE time due to the smaller slice select gradient. A 3D sequence excites a thick slice or slab and uses slice gradient phase encoding to spatially localize signal in the direction of the thick slice, whereas a 2D sequence uses slice selective excitation alone to spatially localize in the slice direction. Slice thickness in a 3D sequence is defined by:



$$\text{Slice Thickness} \approx \text{TH}_{\text{slab}} / N_{\text{pe slice}} \quad (2-3)$$

where  $\text{TH}_{\text{slab}}$  is the excitation slab thickness and  $N_{\text{pe slice}}$  is the number of phase encodes in the slice direction. To obtain a thin slice with an appropriate profile in a 2D sequence requires the use of a long duration soft pulse with high strength magnetic gradients. This becomes impractical in terms of other parameters such as the echo time, which will be discussed later. Another problem with obtaining thin slices from a 2D sequence lies in the signal-to-noise ratio (SNR) [8-10]. The SNR is defined as the signal divided by the standard deviation of the noise and can be described for a 2D sequence by the equation [7,11] :

$$\text{SNR}_{2\text{D}} = \frac{\text{TH}_{\text{slice}} \text{FOV}_{\text{freq}} \text{FOV}_{\text{pe}}}{N_{\text{freq}} N_{\text{pe}}} \sqrt{\frac{N_{\text{freq}} N_{\text{pe}}}{\text{BW}_{\text{rec}}}} \quad (2-4)$$

where  $\text{TH}_{\text{slice}}$  is the slice thickness and  $\text{BW}_{\text{rec}}$  is the receiver bandwidth. For a 3D sequence the SNR can be described with the equation [7,11]:

$$\text{SNR}_{3\text{D}} = \frac{\text{TH}_{\text{slab}} \text{FOV}_{\text{freq}} \text{FOV}_{\text{pe}}}{N_{\text{pe slice}} N_{\text{freq}} N_{\text{pe}}} \sqrt{\frac{N_{\text{pe slice}} N_{\text{freq}} N_{\text{pe}}}{\text{BW}_{\text{rec}}}} \quad (2-5)$$

Where  $N_{\text{pe slice}}$  is the number of phased encodes steps in the slice direction. Thus, when parameters such as TR and flip angle are kept constant, the 3D has better SNR



by a factor of  $(N_{pe \text{ slice}})^{1/2}$ . For these reasons, further discussion will be limited to the 3D pulse sequence.

### 2.3 The 3D TOF MRA pulse sequence

The timings of both RF and gradient pulses for a single TR of the 3D TOF MRA are shown in Fig. 2-2. The following discussion shall focus on the aspects of the sequence, which relate specifically to MRA.

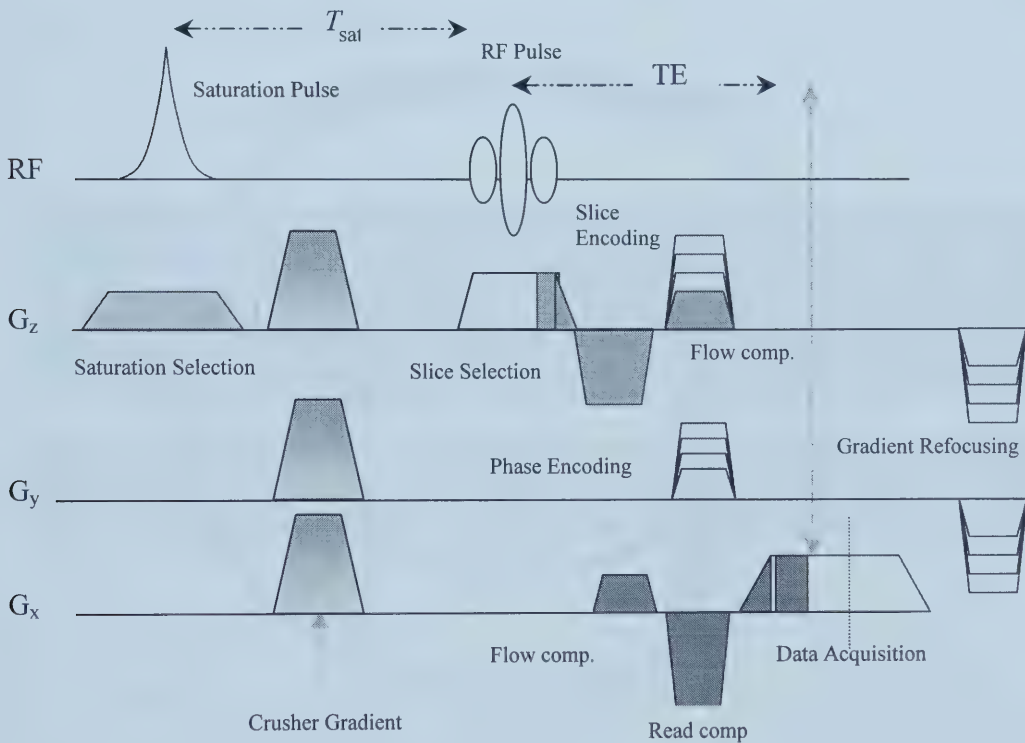


Figure 2-2.

*A 3D TOF MRA sequence with venous saturation and flow compensation in the slice and frequency direction.*





### 2.31 Venous Suppression and the Saturation Pulse

It is often advantageous in MRA to either image the arteries or the veins. To facilitate this, a saturation pulse excitation slab is positioned either above or below the imaging slab [7,12]. By applying a  $90^\circ$  pulse every TR and spoiling the transverse magnetization using crusher gradients, the magnetization of the target blood is saturated before entering the imaging slab. In the case of venous suppression, the saturation slab is placed above the imaging slab (Fig 2-3) saturating the venous signal prior to it entering the imaging slab.

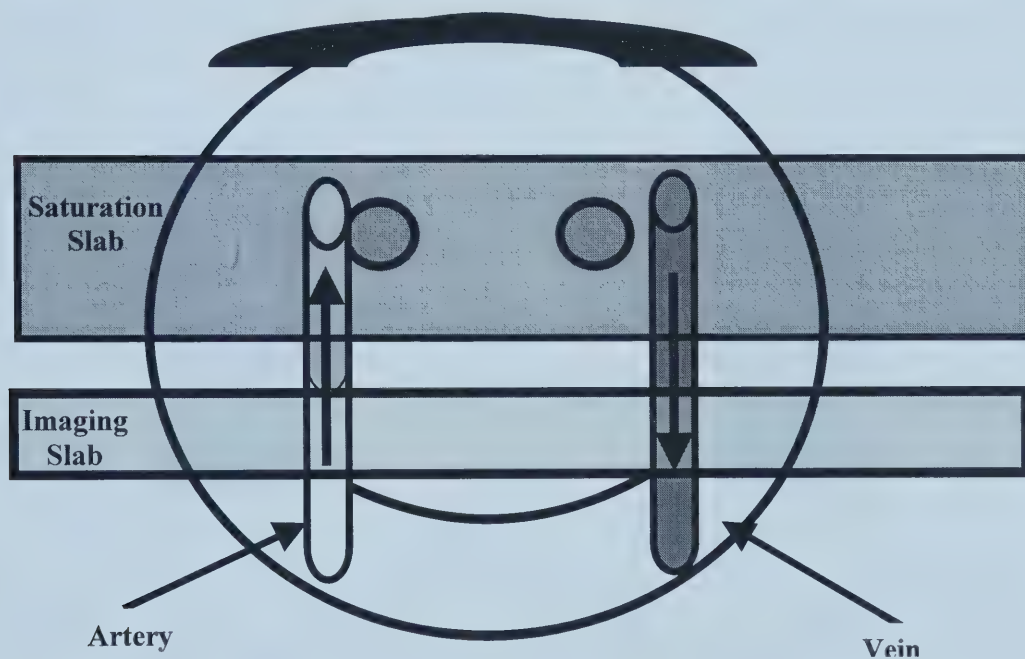


*Figure 2-3 By exciting a slab superior to the imaging slab it is possible to suppress venous blood signal entering the imaging slab.*

The result of this is that only arterial blood enters the imaging slab with undisturbed  $M_z$  magnetization.



### 2.32 Excitation and the Ramp Pulse

Because 3D imaging excitation slabs are relatively thick (usually around 30 mm), saturation of the blood signal as it travels through the excitation slab becomes significant.

To deal with this, an RF pulse with a linearly ramped frequency profile is used to excite the blood as seen in (Fig. 2-4) [13]. In the presence of the slice select gradient, the frequency profile becomes the spatial excitation profile in the slice select direction.

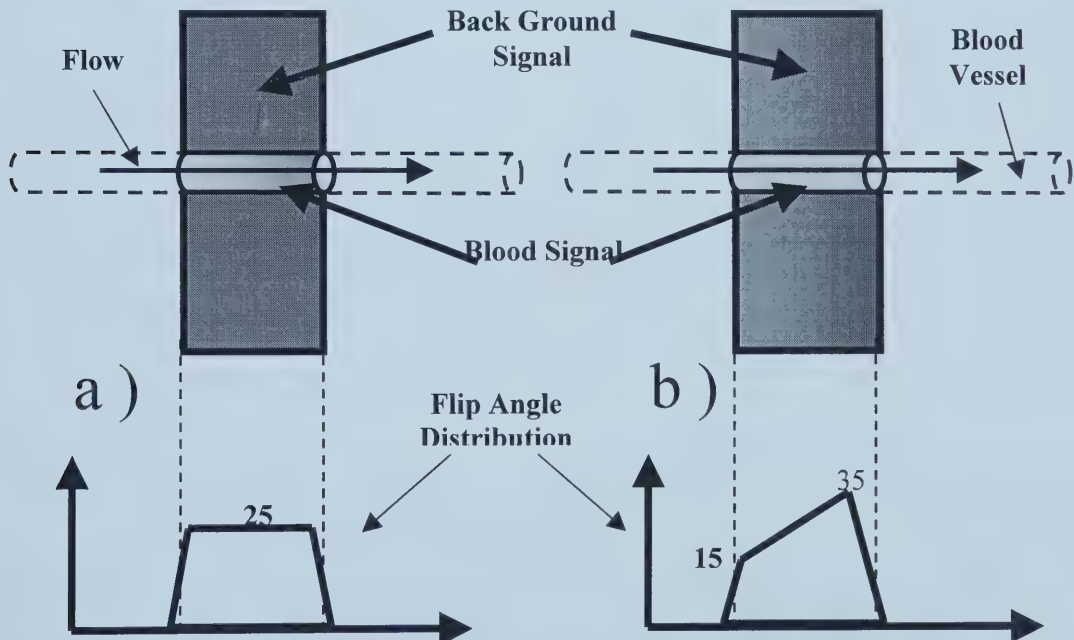


*Figure 2-4*  
when using a regular soft pulse in TOF MRA blood signal of the blood depletes as blood moves through the imaging slab due to successive excitation pulses a.). By using a ramp profile a more uniform signal distribution can be obtained b.).



Thus the  $M_z$  is used in a manner, which provides a more even blood signal distribution across the slab [14]. With a ramp pulse it is important to note that although the difference in blood signal changes less across the slab, there will be a variation in background signal depending on the delivered flip angle in the region of interest. Contrast is defined as:

$$\text{Contrast} = (\text{Blood Signal} - \text{Background Signal}) / \text{Background Signal} \quad (2-6)$$

Thus with the ramp pulse contrast is not linear across the imaging slab due to the decrease of background signal across the slab.

### **2.33 Flow Compensation**

The position of flowing blood flowing with constant velocity in the **X** direction can be described by:

$$x = x_0 + v_x t \quad (2-7)$$

where  $x_0$  is the X displacement at time  $t=0$  and  $v_x$  is the velocity in the **X** direction.

Thus phase acquired over the application of a gradient becomes:



$$\Theta = \gamma \int_{\mathbf{x}} (G_x(t) \bullet (\mathbf{x}_0 + \mathbf{v}_x t)) dt \quad (2-8)$$

The result of this is that moving spins can accumulate additional phase, which can result in ghosting of pulsatile blood as well as increased signal dropouts due to intravoxel dephasing when there are multiple velocity components within a single voxel. In order to compensate for this, an additional gradient lobe is added such that zero and first order moment satisfy:

$$\text{Moment}_{\text{zero}} = \int G_x(t) dt = 0 \quad (2-9a)$$

$$\text{Moment}_{1\text{st}} = \int t \bullet G_x(t) dt = 0 \quad (2-9b)$$

where  $\tau$  is defined as the time between the start of the initial gradient lobe and the time when the center of k space is sampled. Satisfying these two equations ensures that all stationary spins are refocused at the center of k space and also that spins traveling at a constant velocity are refocused at the center of k space [15].

### **2.34 Suppression of Fat signal & Echo Time.**

The difference between the fat and water resonance is 3.5 ppm, which translates to 220 Hz [14] at 1.5 T and 440 Hz at 3.0 Tesla. By choosing an appropriate echo time, it possible to sample the center of K space while fat and water are 180° out-of-phase





(TE = 1.14, 3.4, 5.7, and 7.9 msec) (see Fig 2-5 a). At the out-of-phase condition, the magnetization from both water and fat will oppose each other producing a much-reduced signal (Fig 2-4 b). It is thus possible to reduce the signal from fat by the appropriate choice of echo times.

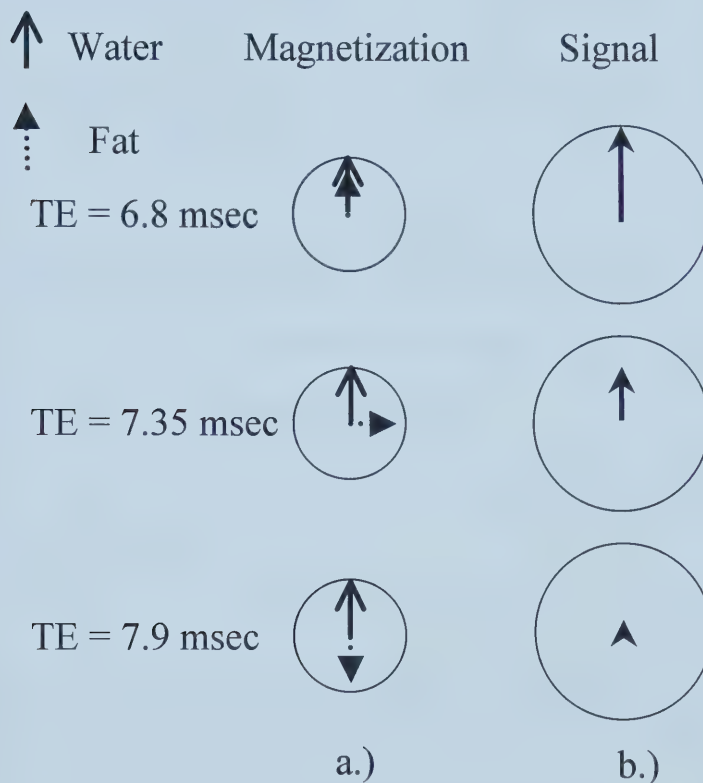


*Figure 2-5 Because of the chemical shift in fat it is possible to suppress fat signal b.) by choosing an echo time when fat and water are  $180^\circ$  out-of-phase a.). The times shown above are for a 3.0T magnetic field strength.*



## 2.4 References

1. Suryan, G., *Nuclear resonance in flowing liquids*. Proc Indian Acad Sci, 1951. **33**: p.107-111.
2. Singer, J.R., *Blood flow rates by nuclear magnetic resonance measurements*. Science, 1959. **130**: p. 1652-1653.
3. Morse, O.C. and J.R. Singer, *Blood velocity measurement in intact subject*. Science, 1970. **170**: p. 440-441.
4. Keller, P.J., *et al.*, *MR angiography with two-dimensional acquisition and three-dimensional display*. Radiology, 1989. **173**: p. 527-532.
5. Haacke, E.M., *Magnetic Resonance Imaging, physical principles and sequence design*. 1999: John Willey & Sons.
6. Brown, M.A., Semelka R.C., *MRI Basic Principles and Applications*. 1995: John Wiley & Sons.
7. Dumoulin, C.L., *et al.*, *Three-dimensional time-of-flight magnetic resonance angiography using spin saturation*. Magn Reson in Med, 1989. **11**: p. 35-46.
8. Carlson, J., *et al.*, *Signal-to-noise ratio and section thickness in two-dimensional versus three-dimensional Fourier Transform MR imaging*. Radiology, 1988. **166**: p.266-270.
9. Edelstein, W.A., *et al.*, *Signal, noise, and contrast in nuclear magnetic resonance (NMR) imaging*. J Comput Assist Tomogr, 1983. **7**: p. 391-401.
10. Parker, D.L. and G.T. Gullberg, *Signal-to-noise efficiency in magnetic resonance imaging*. Med Phys, 1990. **17**: p. 250-257.



11. Kaufman, L., *et al.*, *Measuring signal-to-noise ratios in MR imaging*. Radiology, 1989. **173**(1): p. 265-267.
12. Potchen, E., *et al.*, *Magnetic Resonance Angiography: Concepts and Applications*. 1993, St. Louis: Mosby.
13. Atkinson, D.J., *et al.*, *Improved MR angiography:magnetization transfer suppression with variable flip angle excitation and increased resolution*. Radiology, 1994. **190**: p. 890-894.
14. Nagele, T., *The effect of linearly increasing flip angles on 3D inflow MR angiography*. Magn Reson Med, 1994. **31**: p. 561-566.
15. Weisskoff, R.M., A.P. Crawley, and V. Wedeen. *Flow sensitivity and flow compensation in instant imaging. Abstracts of the SMRI*. 1990. New York.



## Chapter 3

# Modulated Magnetization Transfer TOF MRA\*

### 3.0 Introduction

At standard clinical field strengths of 1.5 T and lower, pulsed magnetisation transfer (MT) has been shown to be an effective way to further suppress background signal in three-dimensional (3D) time-of-flight (TOF) MR angiography (MRA) (1-5). Owing to the large RF power requirements of MT, it must be applied carefully to stay within the allowed specific absorption rate (SAR). At higher field strength, implementation of the MT technique becomes more problematic because the SAR increases with the square of the RF transmission frequency, which is proportional to the main magnetic field strength. For this reason, initial publications at 3.0 T on TOF MRA have not made use of MT (6,7). However, the fact that MT can be performed at 3.0 T has been recognised (6,8,9). In this note, we demonstrate effective use of MT at 3.0 T by combining modulation of the pulsed MT flip angle during the acquisition (8), with an altered phase encode order in order to keep the 8-second time-averaged SAR under 3 W/kg throughout the acquisition time. The technique is demonstrated first in phantom studies, and then applied to 3D TOF MRA of the distal middle cerebral arteries in seven normal volunteers at 3.0 T.

*\* A version of the chapter has been submitted as a paper to the Journal of Magnetic Resonance Imaging.*





### 3.1 Materials and Methods

In order to model the signal response at 3.0 T to pulsed MT, a phantom was created of 4% agar by weight (10) with a longitudinal relaxation time of 1.2 s. Pulsed MT was added to a standard 3D TOF MRA sequence at 3.0 T by applying a 10 ms gaussian pre-excitation pulse within each repetition time (TR) at 1700 Hz off-resonance (4). With all phase encoding turned off, the 3D TOF MRA sequence was run using a fixed TR of 36 ms. The amplitude of the MT pulse was modulated between each TR and the resultant MR signal was recorded. For phantom studies, the peak amplitude of the MT pulse corresponded to an equivalent on-resonance excitation pulse of  $1200^\circ$ . Throughout data acquisition, a rolling 8-second average SAR reading was recorded every 120 ms. The SAR was determined in a standard manner from the difference between measured forward and reverse power via directional couplers and also accounted for cable losses and coil coupling efficiency (11). The results from the phantom study were then used in the implementation of MT in a standard 3D TOF MRA imaging sequence (shown in Fig 3-1) for volunteers.

For *in vivo* experiments, the amplitude of the MT pulse was modulated over time such that the greatest MT contrast was achieved for the central portion of k-space (8). The modulation was performed such that the maximum MT effect could be achieved while maintaining the 8-second rolling SAR average below 3W/kg. The phase encoding order used the slice select direction ( $k_z$ ) as the outer loop, and the



phase encode direction ( $k_y$ ) as the inner loop (shown in Fig 3-2) such that a central line of  $k_y$  was passed through every  $(TR \cdot N_y)$ , or every 9.2 s, where  $N_y$  is the number of  $k_y$  phase encoding steps.

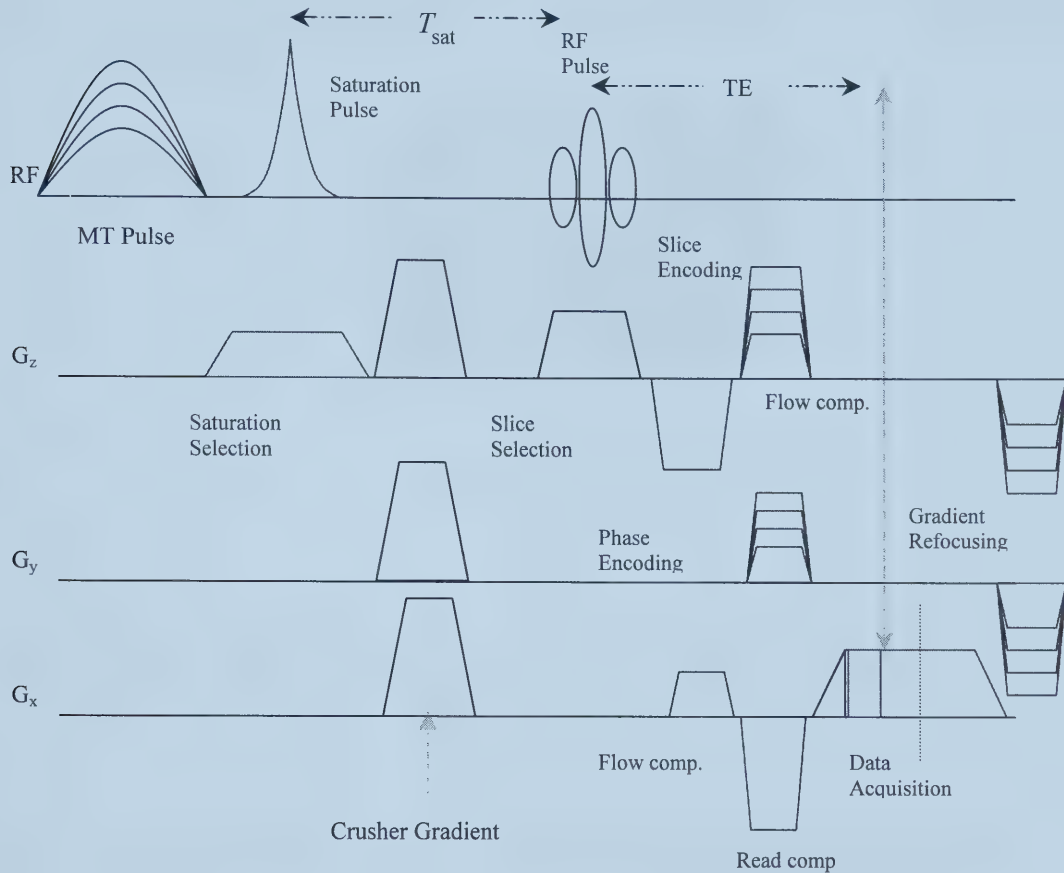


*Figure 3-1.*  
Modulated MT 3D TOF MRA sequence with flow compensation in the slice and frequency directions and spatially selective venous suppression pulse.

This ordering method allowed enough phase encodes for the MT modulated background signal to reach its lowest value before the middle of  $k_y$ -space is reached on each pass through a constant  $k_z$  value. Furthermore, it assured that the



application of MT was spread out across the complete acquisition time to minimize the rolling 8-second RF power average.

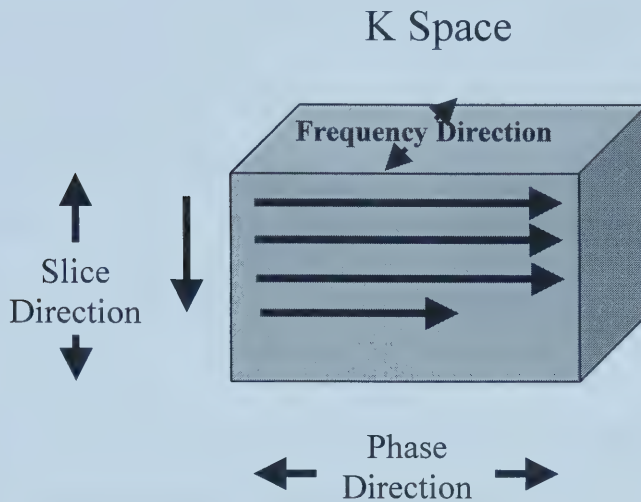


Figure 3-2.

*The phase encode order is set such that all phase increments for one slice phase encode are made before the phase encode is incremented in the phase direction.*

Before beginning the acquisition, the pulse multiplier for the MT amplitude was determined for each volunteer using real-time feedback from the SAR monitor to approach but not exceed the allowed 3 W/kg. For determination of head SAR, the weight of the head and neck within the RF coil was computed by taking a conservative 5% of the total body weight.

Three-dimensional TOF MRA images were acquired at 3.0 T from 7 volunteers (mean age  $29 \pm 6$ ) both without MT and with the modulated MT approach.



Informed consent was obtained from all subjects. The 3D TOF MRA sequences used the following parameters: TE/TR of 7/36ms, ramped RF excitation, venous suppression, and 1<sup>st</sup> order moment nulling in the slice and frequency directions. The matrix size was 512 x 256 x32 in frequency, phase and slice directions respectively, using a 20 cm in-plane FOV in the x and y directions and a 32 mm slab thickness giving 1mm slices. The images were acquired over two slabs using a standard MOTSA technique (12). A 26 cm diameter homebuilt quadrature transmit-receive head coil was used which had a 75% coil coupling efficiency.

For comparison purposes, the same 7 volunteers were also imaged at 1.5 T with and without MT using a standard 3D TOF MRA sequence. The 1.5 T sequence made use of similar parameters to the 3.0 T sequence, except steady-state MT was used. Images from both 1.5 T and 3.0 T were reconstructed and normalized in the same manner. Measurements of blood signal were taken from a region-of-interest (ROI) along the M2 branch of the middle cerebral artery (MCA) in the collapsed image. Background ROI measurements for signal and noise were averaged over the middle source images in the left and right posterior temporal and occipital regions. In measuring MT contrast for individual tissue types, the source images corresponding to a flip angle of 20° along the excitation ramp pulse were used. This lower flip angle location within the ramp pulse was subject to less RF saturation, which made distinction between tissue types straightforward.





### 3.2 Results

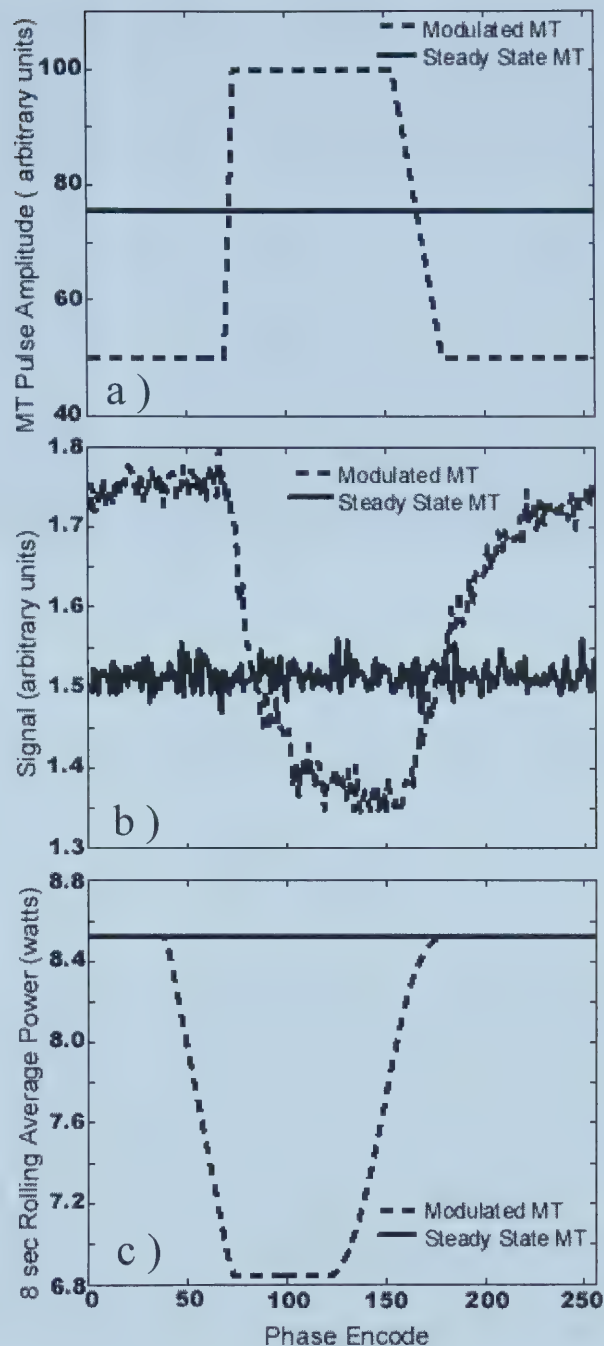
Figure 3-3a shows the modulation used for the MT pulse amplitude at 3.0 T. The full MT pulse amplitude is used for only 30% of the acquisition, with the remaining time mainly at half-maximum. The steady-state MT amplitude for the same maximum 8-s SAR is also shown. The resulting background signal is shown in Fig. 3-3b for the modulated and steady state MT approaches using the 4% agar phantom. The central MT region has a 10% decrease in background signal when using modulated MT. As shown in Fig. 3-3c, SAR values change in accordance with the amplitude multiplier of the MT pulse and range between 6.8 W and 8.5 W. Peak SAR values, over any 8 s period are the same for both the modulated and steady state MT schemes even though a higher maximum flip angle is used in the modulated scheme. If the SAR values are summed over the complete acquisition, the modulated MT has a total SAR that is 92% of the steady state method.

Figure 3-4 shows 3D TOF source images from a volunteer acquired at 3.0 T in (a) without and (b) with modulated MT. The decrease in the background signal with use of modulated MT is evident. Within a slice receiving a 20° flip angle, average signal intensities over all seven volunteers showed decreases of  $0 \pm 8 \%$  for cerebrospinal fluid,  $52 \pm 5 \%$  for white matter and  $40 \pm 8 \%$  for grey matter when modulated MT was used.

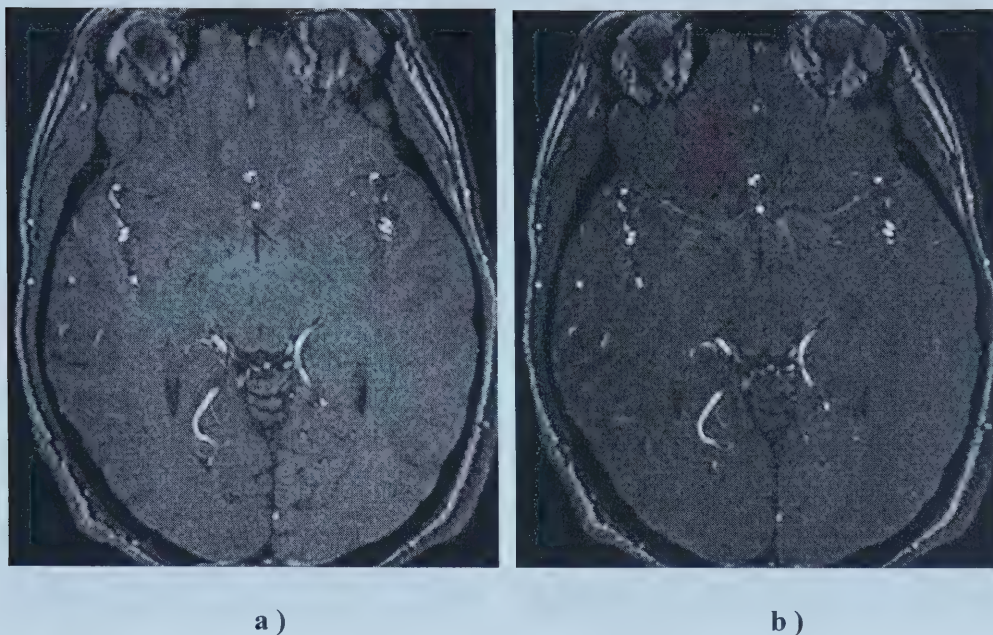


Figure 3-3

The MT pulse amplitude for each phase encode in the ky direction for both the steady and modulated MT schemes is shown in (a). In both cases, the maximum 8 s SAR is the same. The slight asymmetry in the MT modulation is employed to give better symmetry in the signal response. (b) The resultant transverse magnetization for both the steady state and modulated MT sequences is shown. The modulated sequence has ~10% less signal than the steady state sequence over the central values of k-space. The 8 s rolling average power for both steady state and modulated MT are plotted in (c). Although the peak average power is the same for both schemes, the total power deposited is approximately 8% lower for the modulated MT scheme.







*Figure 3-4*

*Source images obtained at 3.0 T with the 3D TOF sequence (a) without MT, (b) with modulated MT. Note the substantial improvement in background suppression when using MT.*

Figure 3-5 shows signal variation across the imaging slab within source images for both MT (a,b) and non MT (c,d) pulse sequences. Slices b) and d) correspond flip angle of 18 degrees and slices a.) and c) correspond to a flip angle of 33 degrees. Across the slices in the imaging volume, the background signal variation due to the ramp excitation pulse was 16.4% for the non-MT sequences and reduced to 5.8% with the application of modulated MT.





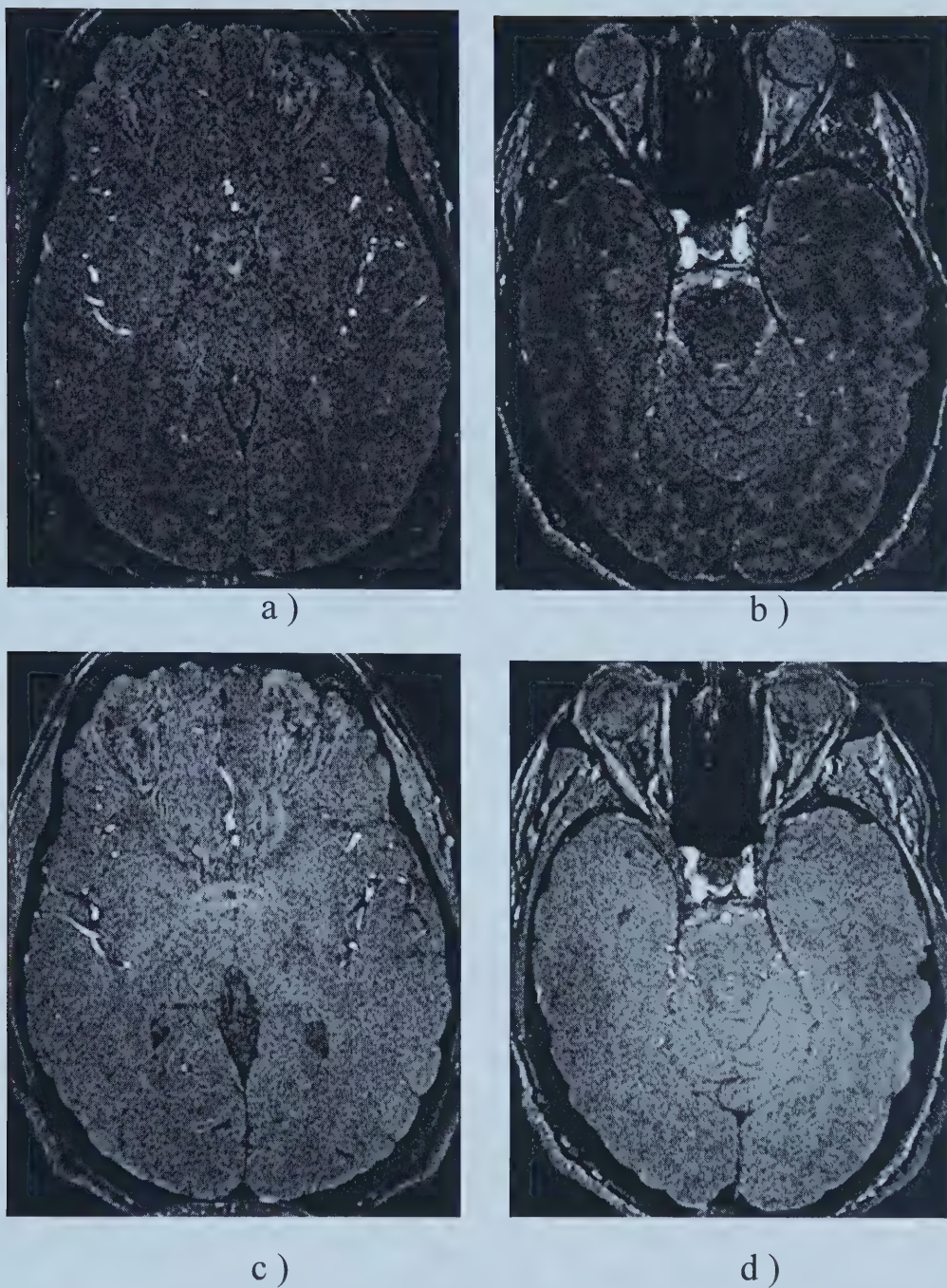


*Figure 3-5*

*Shows the increased effectiveness of MT at low excitation pulse flip angle and the resultant decreases signal variation across the imaging slab with the use of MT (a,b) vs non MT (c,d). Images (b,d) correspond to a flip angle of 18 degrees and (a,c) correspond to a flip angle of 33 degrees.*





Figure 3-6 shows collapsed images of the distal right middle cerebral artery from a different volunteer. Figures 3-6 a,b were acquired at 1.5 T, (a) without and (b) with MT. Similarly Figs. 3-6 c,d were acquired at 3.0 T, (c) without and (d) with modulated MT. In all the images, the same rectangular 3D volume was used to perform the collapse. The 3.0 T modulated MT sequence shows improved detection of small vessels as compared to the 3.0 T sequence without MT, which in turn, was preferable to the 1.5 T methods. A comparison of all of the results at 1.5 T and 3.0 T is shown in Table 1 for blood-to-background contrast in the M2 branch of the MCA. The results indicate an increase corresponding to both field strength and to the use of MT. For the contrast-to-noise ratio, the increase corresponds to field strength, but there is a decrease with use of MT.

Table 3-1

**Blood-to-Background Measurements at 1.5 T and 3.0 T from a Distal  
Intracranial Vessel**

Field Strength	Normalized Contrast*	Contrast-to-Noise Ratio
1.5T no MT	$2.8 \pm 0.6$	$34 \pm 6$
1.5 T with MT	$3.3 \pm 0.6$	$33 \pm 5$
3.0T no MT	$4.0 \pm 0.6$	$66 \pm 11$
3.0T with MT	$6.0 \pm 0.8$	$63 \pm 14$

\* Normalised contrast = (blood-background)/background



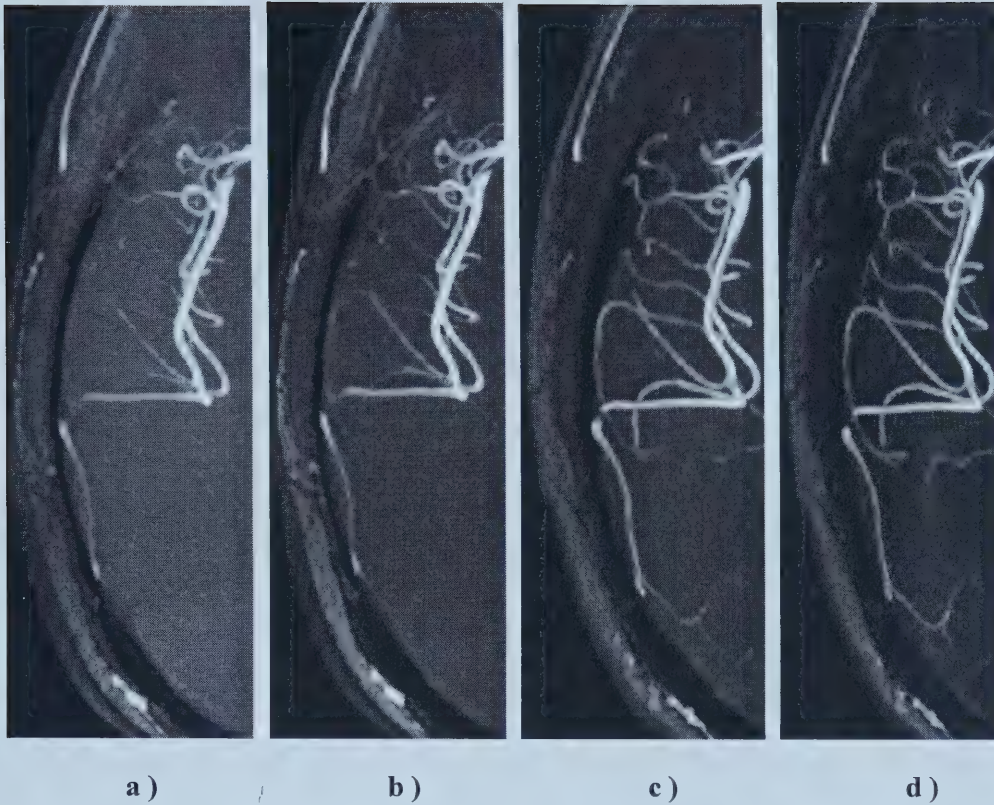


**Figure 3-6**

*The collapsed images illustrate the distal middle cerebral arteries acquired with and without MT at 1.5 T and 3.0 T. (a) 1.5 T without MT, (b) 1.5 T with MT, (c) 3.0 T without MT, and (d) 3.0 T with MT. Immediately noticeable is the increase in small vessel detection resulting from the use of MT and higher field.*

### **3.3 Discussion**

The modulation of MT across each line of  $k_y$  acts as an edge enhancement filter for those tissues experiencing MT contrast, and could result in a vessel being blurred by neighboring background signal (8). To lessen the potential for image distortion, half strength MT pulses are applied throughout the outer portions of k-space. In simulations and in vivo, artifactual effects of this filter were found to be minimal.



Hence, for the volunteer experiments, the modulated MT approach was used to achieve superior background suppression over steady state MT for the given SAR threshold.

For the volunteer experiments, the MT modulation made use of a maximum flip angle of  $1100^\circ \pm 150^\circ$  which is similar to maximum flip angles used at 1.5 T. The maximum average power delivered over any 8 s was  $11.3 \pm 1.4$  W. The modulated MT scheme used here reduces the total SAR by a factor of 1.9 over continual application of the maximum flip angle. However, continual application of this maximum flip angle would exceed the allowable SAR. The SAR was also reduced somewhat by using a 10 ms gaussian pulse for MT at 3.0 T, as opposed to a 7 ms version at 1.5 T. The FDA guidelines allow 3 W/kg over a 6 min period and up to 9 W/kg for a 10 s period (9). For our work 3 W/kg was maintained over any 8 s period.

In conclusion, we have demonstrated implementation of pulsed MT for 3D TOF MRA at 3.0 T with significantly improved background suppression while maintaining SAR under 3 W/kg as measured by an 8 s average. This was accomplished by modulation of the MT pulse amplitude in conjunction with the reordering of the phase encode order to maximize effective MT contrast for the given SAR limit.



### 3.4 References

1. Balaban RS, Ceckler TL. *Magnetization Transfer Contrast in Magnetic Resonance Imaging*. Magnetic Resonance Quarterly 1992;8:116-137.
2. Edelman RR, Ahn SS, Chien D, Li W, Goldmann A, Mantello M, Krammer J, Kleefield J. *Improved Time-of-Flight MR Angiography of the Brain with Magnetization Transfer Contrast*. Neuroradiology 1992;184:395-399.
3. Pike GB, Hu BS, Glover GH, Enzmann DR. *Magnetization transfer time-of-flight magnetic resonance angiography*. Magn Reson Med 1992;25:372-379.
4. Graham SJ, Henkelman RM. *Pulsed Magnetization Transfer Imaging: Evaluation of Technique*. Radiology 1999;212:903-910.
5. Wolff SD, Balaban RS. *Magnetization Transfer Imaging: Practical Aspects and Clinical Applications*. Radiology 1994;192:593-599.
6. Bernstein MA, Huston J, Lin C, Gibbs GF, Felmlee JP. *High-resolution intracranial and cervical MRA at 3.0T: technical considerations and initial experience*. Magn Reson Med in press.
7. Al-Kwif O, Emery DJ, Ferdinandy R, Wilman AH. *Exploiting three tesla for circle of willis and carotid artery time-of-flight MR angiography: a quantitative, experimental and theoretical study*. In: Proceedings of the 9th Annual Meeting of ISMRM, Glasgow, Scotland, 2001. p 299.





8. Parker DL, Buswell HR, Craig K, Alexander AL, Keck N, Tsuruda JS. *The Application of Magnetization Transfer to MR Angiography with Reduced Total Power*. Magn Reson Med 1995; 34:283 - 286.
9. Hugg JW, Bernstein MA, Stokar S, Lin C, Rosenfeld D, Felmlee JP, Montag A, Huston JH, Assif B, Reynolds HG. *Routine Clinical Head MRI at 3.0T with Optimized RF Power Management*. In: Proceedings of the 9th Annual Meeting of ISMRM, Glasgow, Scotland, 2001. p 1349.
10. Graham SJ, Henkelman RM. Understanding Pulsed Magnetization Transfer. JMRI 1997; 7:903-912.
11. Felmlee JP, Bernstein MA, Huston J. *Analysis of RF heating at 3.0T*. In: Proceedings of the 8th Annual Meeting of ISMRM, Denver, USA, 2000. p 2002.
12. Parker DL, Yuan C, Blatter DD. *MR angiography by multiple thin slab 3D acquisition*. Magn Reson Med 1991; 17:434-451.



## Chapter 4

# Magnetization-Prepared Time of Flight MR Angiography

### 4.0 Introduction

Conventional 3D time-of-flight MR Angiography (TOF MRA) has proven to be a good technique for imaging vessels with steady flow such as normal intracranial arteries[1]. It has been less successful in imaging vessels with pulsatile flow such as the carotid arteries. In this region, TOF MRA regularly overestimates the degree of stenosis. Problems arise due both to physical movement of the vessel over the cardiac cycle [3], variable flow through the cardiac cycle [2] and intravoxel dephasing due to complex flow mainly during systole. These problems can be partially solved through diastolic image acquisition using cardiac triggering. However, cardiac triggering would break up the steady-state magnetization needed for standard TOF MRA. Magnetization-Prepared 3D MR Angiography (MP MRA) [4,5] is well suited to cardiac triggering and presents a possible solution to the problems that exist with TOF MRA in pulsatile regions. Performing the procedure at 3.0 T may be advantageous to 1.5 T due both to the intrinsic T1 increase and to the increased signal-to-noise ratio (SNR) that exists at higher magnetic field.

Like standard TOF MRA, MP MRA relies on the inflow of blood with unperturbed longitudinal magnetization to provide high blood signal. Where the techniques differ



is in the manner in which they suppress surrounding tissue. Instead of using repetitive small flip angle pulses to deplete background magnetization, MP MRA uses a spatially selective inversion pulse to invert the longitudinal magnetization ( $M_z$ ), and then waits for T1 relaxation to approximately null the  $M_z$  prior to an excitation pulse. During this relaxation time, blood with unperturbed  $M_z$  flows into the imaging slab. At the null point, the slab is imaged using a low flip angle excitation pulse. Because the image is acquired at the null point of the background tissue, only the blood will have significant  $M_z$  to contribute to the signal acquired for the image. Figure 4-1 illustrates this process.

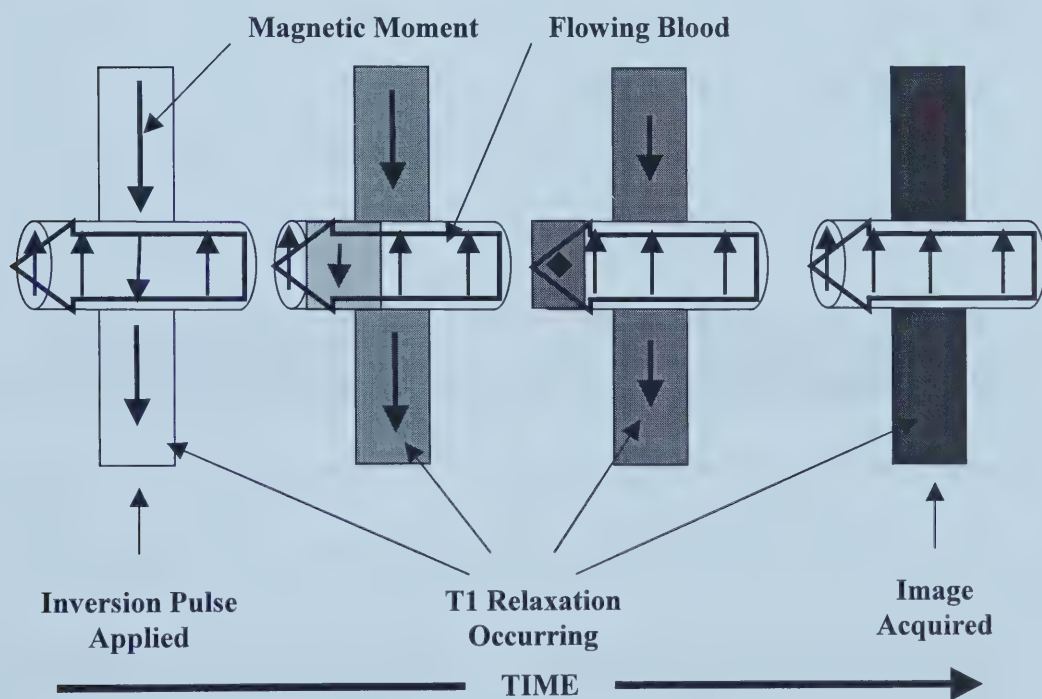


*Figure 4-1*  
The method by which the MP MRA sequence achieves blood-to-background contrast is shown. See text for details.



#### 4.1 3D MP FLASH Sequence.

In the MP MRA sequence, unwanted signals are removed via a preparation phase after which parts of the k-space matrix are sampled. Thus the pulse sequence can be divided into two parts:

- 1) a magnetization-prepared component in which RF and gradient pulses are used to selectively eliminate signal from muscle, fat and venous blood while allowing for fresh blood inflow,
- 2) an imaging component in which a portion of the k-space matrix is sampled.

These two parts alternate during playback with the magnetization-prepared part remaining constant and the imaging part sampling more of k-space during each segment [6]. Figure 4-2 illustrates the time playback.

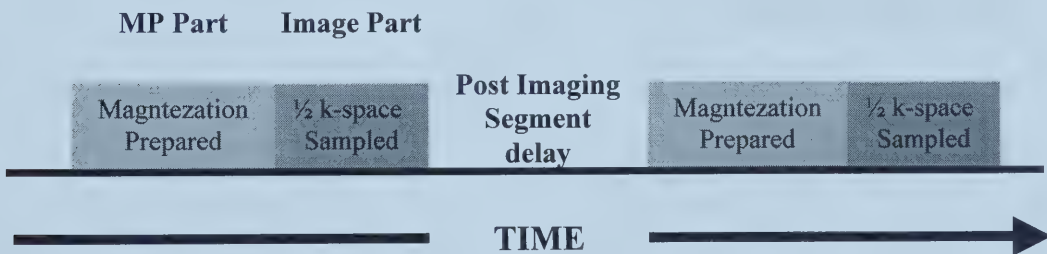


*Figure 4-2*

*The time playback of an MP MRA pulse sequence acquired in two segments.*

The magnetization-preparation and the imaging parts shall be discussed separately in the next sections of this chapter.





## 4.2 Magnetization Preparation and Signal Suppression

Timings of RF and magnetic gradient pulses for the magnetization-prepared part of the MP MRA sequence are shown in Fig 4-3.

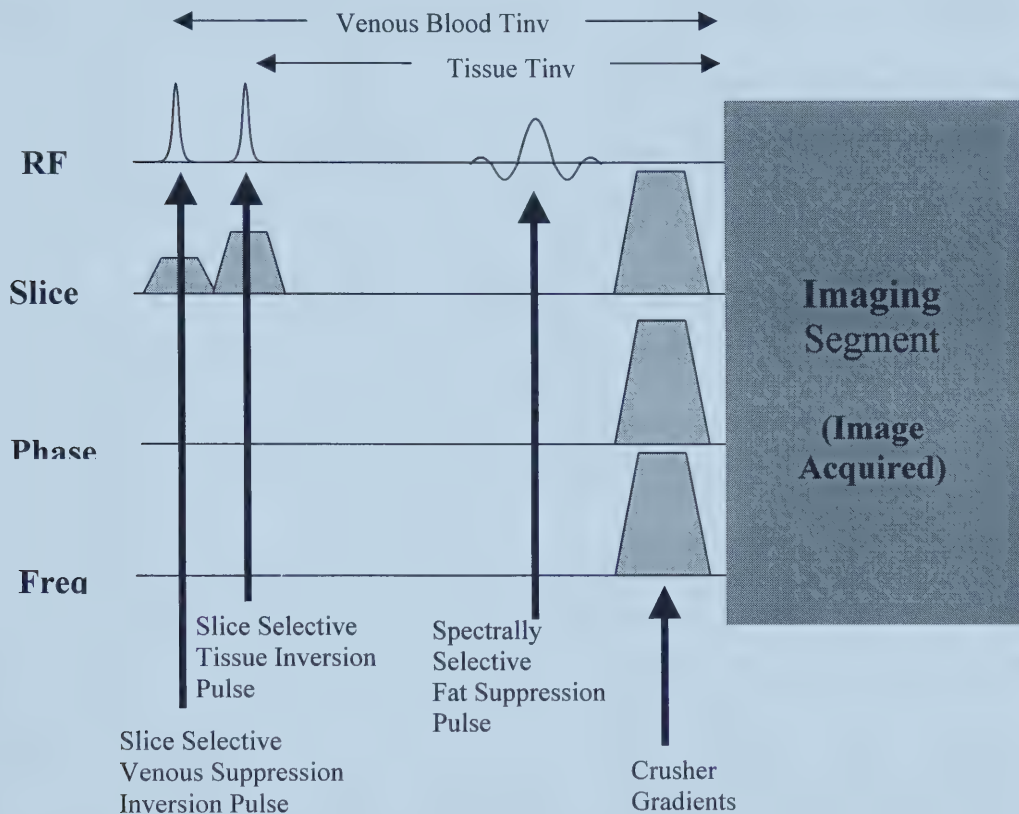


Figure 4-3

Timing diagram for a magnetization-prepared section of a MP MRA sequence with tissue, venous blood, and fat suppression.

The specifics of each suppression method will be discussed in the upcoming sections.



#### 4.21 Inversion Pulse and Tissue Suppression

The majority of tissue suppression comes from the use of a slice selective inversion pulse ( $180^\circ$ ) followed by an inversion time ( $T_{inv}$ ) which is the time between the end of the inversion pulse and the end of the excitation pulse [7,9]. The inversion is achieved by applying a 16 msec, 1400 Hz bandwidth hyperbolic secant RF pulse. The pulse was selected due to its appropriate compromise of high bandwidth and long duration. A high bandwidth allows for a sufficiently large slice gradient to be used to limit the effects of background gradients on distorting the inversion profile. However, the duration must be sufficiently long to allow full inversion of the spins based on the limited available RF amplitude. By varying the  $T_{inv}$ , T1 contrast between tissues can be created. Some examples of contrast available and tissue signal nulls are shown in Fig 4-4. For the application of a single inversion pulse, the null time for a specific T1 can be determined using Eq 1-29 to give:

$$T_{null} = -T1 * \ln(1/2) \quad (4-1)$$

where  $T_{null}$  is the time from the inversion pulse until the point where  $M_z = 0$  for the specific tissue. During an imaging sequence, determining the optimum  $T_{null}$  becomes more complicated because it depends on parameters such as: the imaging TR, the number of views, the flip angle of the excitation pulse, and the time after the imaging part of the sequence before the next inversion pulse is played out. In order to determine optimum  $T_{null}$  for a specific set of pulse sequence parameters, the  $M_z$



magnetization is modeled using Eq 1-26 from Chapter 1. There is an inherent increase in T1 time associated with higher fields [10]. For muscle, which is the primary tissue being suppressed in the case of carotid artery imaging, there is an increase in the T1 from 870 msec at 1.5 T to 1100 msec at 3.0 T. This increase in T1 at higher field correspondingly results in an increase in the  $T_{null}$ .

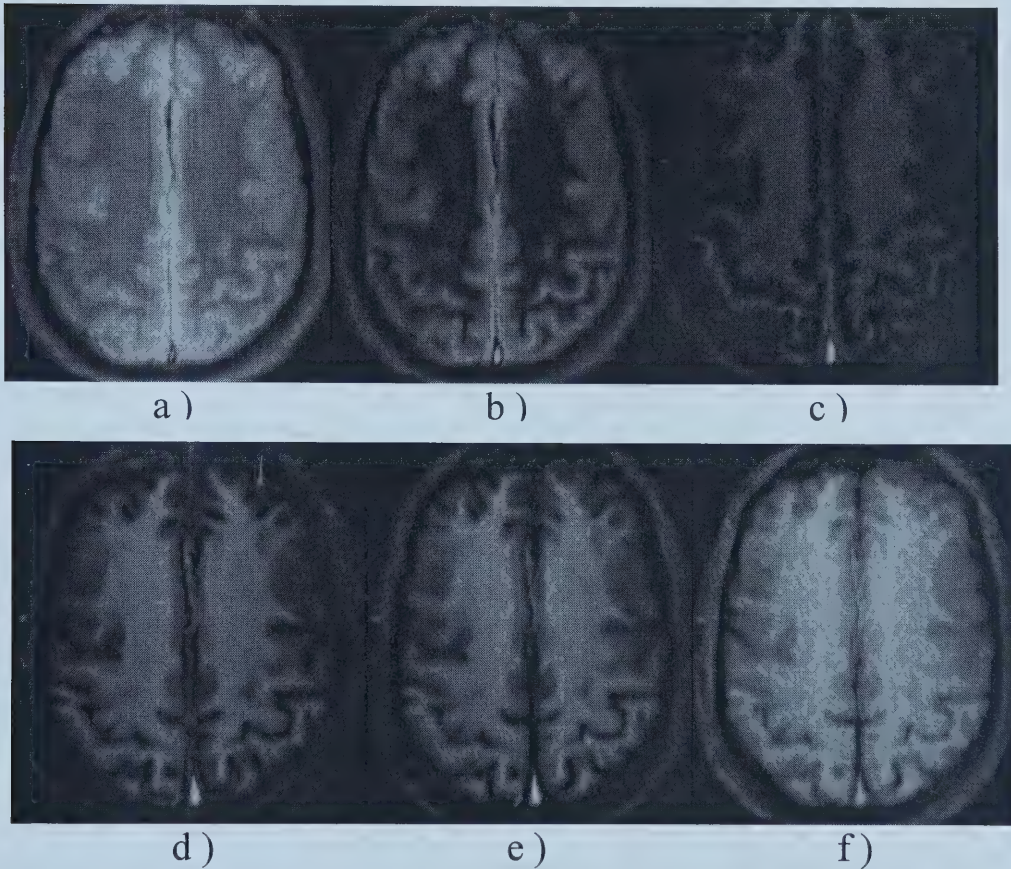


**Fig 4-4**

*This figure gives an example of the ability of an inversion recovery imaging sequence to effectively suppress target tissues. The 3.0 T images were taken with a 2D MP FLASH sequence at different inversion times. a) 200 msec b) 400 msec c) 800 msec d) 1000 msec e) 1200 msec f) 1700 msec. The sequence used TE/TR,*





The increase in  $T_{\text{null}}$  with increasing field for a specific set of parameters is shown in Fig 4-5.

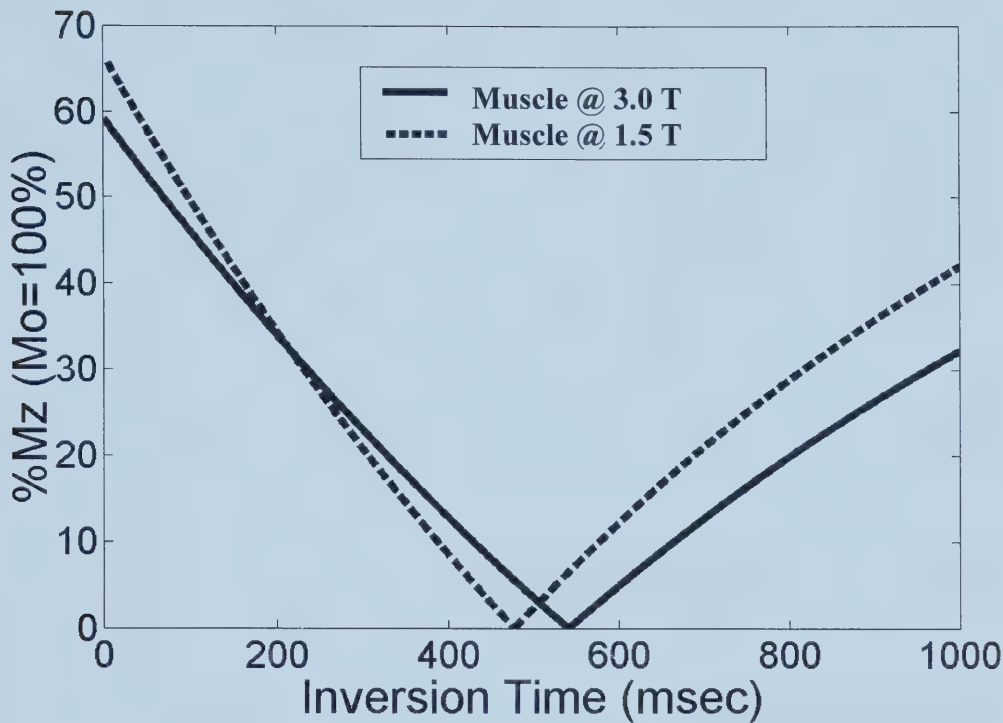


*Figure 4-5*

*Shows available  $M_z$  for different  $T_{\text{inv}}$  for a pulse sequence made with the following parameters:  $TR=10$  msec,  $\text{FlipAngle}=20^\circ$ , 32 views/segment 1000 msec post imaging segment delay, 3 dummy cycles, no T2 dephasing.*

The advantage in a longer  $T_{\text{null}}$  is that  $T_{\text{null}}$  is also the time in which blood flows into the imaging slab. Thus, a longer  $T_{\text{null}}$  results in a better chance for complete arterial blood refreshment.





#### **4.22 Venous Suppression.**

Venous suppression is accomplished in the same manner as tissue suppression. For venous suppression the blood must be inverted prior to it flowing into the imaging slab [9]. Thus, the inversion slab is placed superiorly to the imaging slab. As the venous blood flows into the imaging slab, T1 relaxation is occurring. By the time the imaging slab is sampled, the venous blood is near its null point and thus contributes very little signal to the image. The ideal situation is to invert all blood superiorly to the imaging slab; however, the range of the inversion is often limited by the transmit RF coil coverage. Furthermore, if the inversion pulse is extremely large, the small background gradients may influence the shape of the RF profile. In this work a 10 cm slab is used. A gap of 1.5 cm was used between the tissue and venous suppression inversion slabs to minimize interference between the RF pulses. The center of the venous suppression inversion slab was placed ~8 cm superior to the center of the imaging slab and the imaging slab was 3.2 cm thick. An example of venous suppression is shown in Fig 4-6. The T1 of venous blood is 1200 msec making it just a little longer than that of muscle. It is modeled with the assumption that there is no lasting effect from the imaging segment on the blood. The venous suppression pulse is played out 46 msec prior to the playout of the tissue suppression pulse.



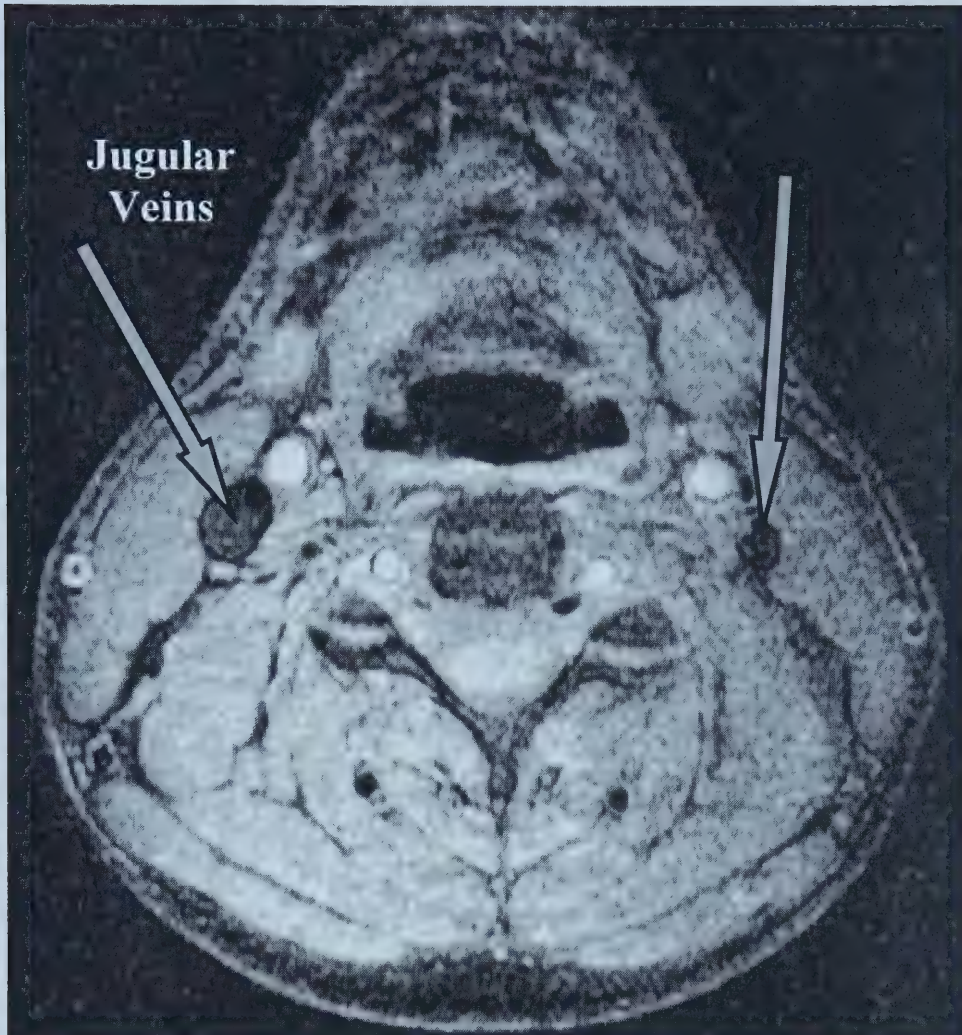


*Figure 4-6*

*By inverting blood superior to the imaging slab it is possible to suppress venous signal entering the imaging slab. The arrows point to the jugular veins. Note: to provide suitable contrast a no  $T_{null}$  inversion time was used in the imaging slab.*



### 4.23 Fat Saturation

Similar to standard TOF MRA, fat saturation takes advantage of the chemical shift property of fat as described in 1.71 of Chapter 1. However, the manner in which these sequences capitalize on this property is different. Standard TOF MRA uses the chemical shift to select an appropriate echo time to obtain fat and water out-of-phase (see 2.34 of Chapter 2). MP MRA uses the chemical shift to selectively excite and spoil fat signal, without affecting the water peak as seen in Fig 4-7. The water-fat chemical shift is 3.5 ppm or 440Hz [9,11] at 3.0 T.

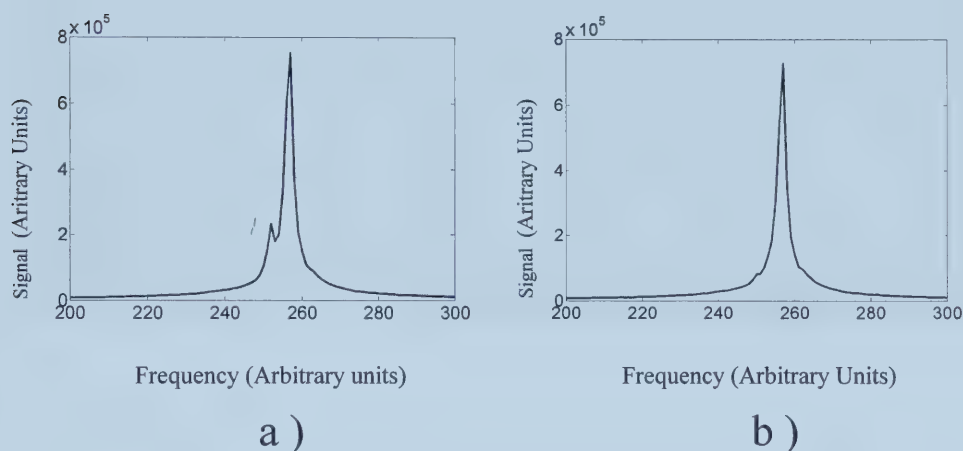


*Figure 4-7*

*Due to the chemical shift, fat signal can be suppressed through use of a narrow bandwidth excitation pulse. a) shows the water fat spectrum using a ninety degree pulse on the water resonance. b) shows the same ninety degree pulse preceded by a fat saturation pulse and spoiler gradients.*

For fat suppression, a 32 msec, 188 Hz bandwidth sinc pulse is played out, without the addition of simultaneous gradients, at an offset from the water resonance peak of





440 Hz. Keeping the bandwidth of the pulse narrow allows for negligible perturbation of the water magnetization. Gradients are then applied in all three directions to dephase the transverse magnetization. The gradients are applied for a short duration (2 msec) to minimize T1 relaxation of the fat to before the excitation pulse of the slab is played out immediately afterward. When the imaging slab is sampled, fat contributes minimal signal to the image as shown in Fig. 4-8.

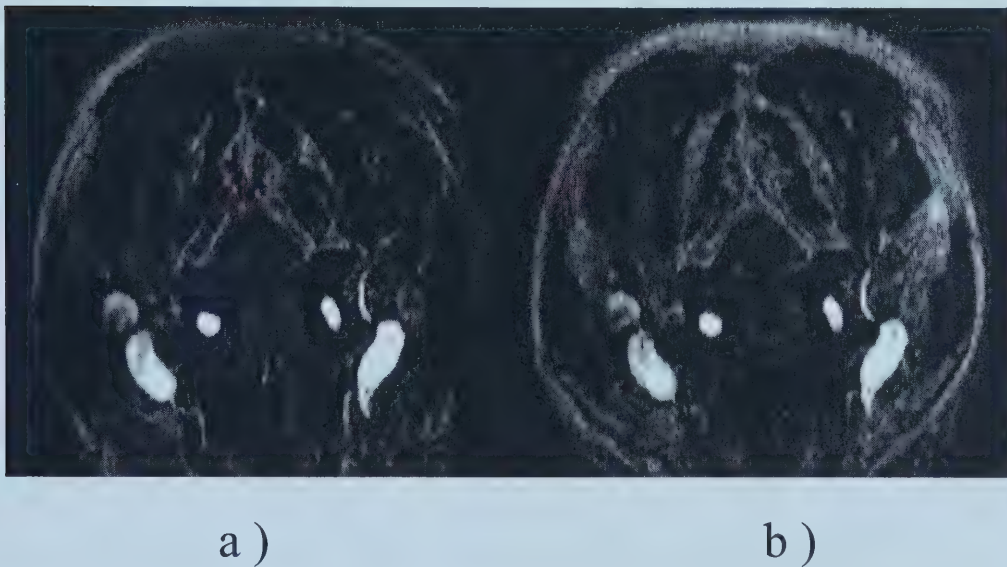


*Figure 4-8*

*The difference in fat signal can clearly be seen in the collapsed images of the neck acquired with a) and without b) the addition of the fat saturation RF pulse and spoiler gradients to the MP MRA sequence.*

#### **4.3 Imaging with FLASH (k space sampling)**

The image acquisition uses a segmented Fast Low Angle SHot (FLASH) play out [12], which is a low angle short TR gradient echo sequence. Timings of RF and





magnetic field gradient pulses for the imaging part of the MP MRA sequence are shown in Fig 4-9.

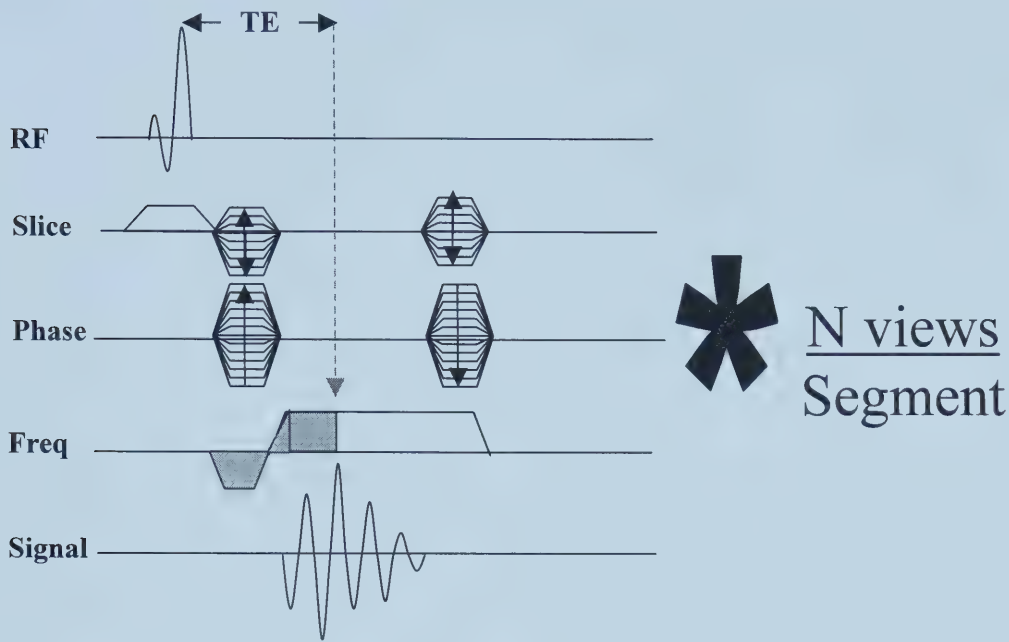


Figure 4-9

*A segmented FLASH sequence with center out slice phase encoding, asymmetrical frequency readout and phase encode rewind gradients.  $N$  views refers to the number of phase encode increments.*

The pertinent parts of the sequence will be discussed in the next sections.

#### 4.31 Minimizing Flow Dephasing through Short TE

Due to the desired cardiac triggered nature of the sequence, a short TR is required in order to fit an adequate number of views within the same phase of the cardiac cycle. This makes flow compensation gradients, as described in Section 2.33 of Chapter 2 impractical due to the resultant increase in TE and hence TR. In addition, by



minimizing TE and imaging during cardiac quiescent intervals, intravoxel dephasing is minimized. By revisiting Eq 2-8 it can be seen that minimizing the TE can minimize the contribution from moving spins to the phase dispersion across a voxel. A minimized TE is accomplished by using strong gradients (20mT/m), fast ramp times (220  $\mu$ sec), 50% asymmetrical frequency [12] readout and a truncated sinc excitation pulse shown Fig 4-10. The price of a truncated sinc is a poorer excitation profile however this is an acceptable trade off for the reduced TE.

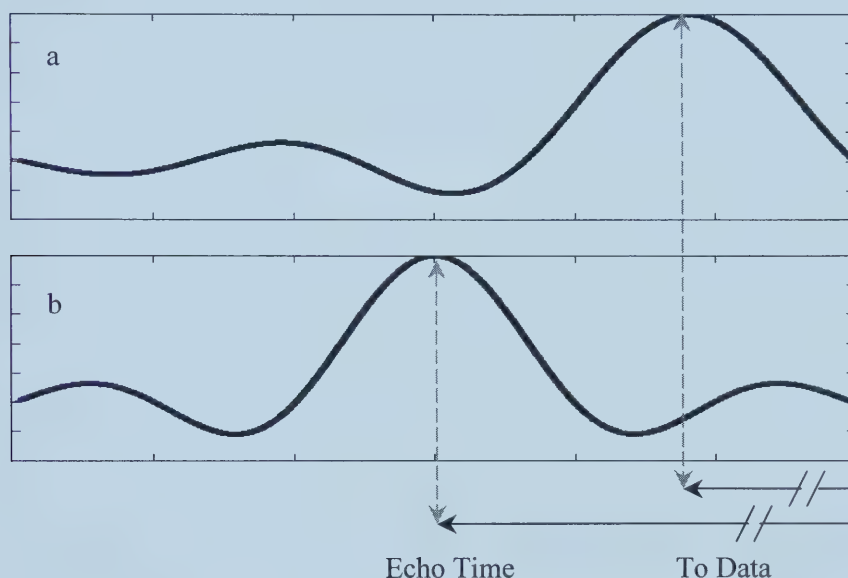


*Figure 4-10*

*By truncating the Sinc pulse a.), TE can be reduced a significant amount as compared to using a non-truncated Sinc pulse b.)*



### 4.32 k space Modulation and Center Out Slice-Phase Encode Order

In our MP MRA sequence, one line of 32 slices or z phase encodes are obtained in a single segment. In the next segment, the y phase encode is incremented and the 32 slice phase encodes are repeated. In order to fit the slice phase encodes of a segment into the quiescent interval in which the blood is to be imaged, the TR must be relatively short ( $TR < 10$  msec); furthermore, no time is afforded to allow dummy scans so that the blood and background may be imaged in the steady state. Thus k-space is sampled during the signal transition to steady state. Because the image is acquired under signal transition, the object's k-space representation is filtered with the fall off (modulation function) in the slice direction. Thus if an object with a profile in the z direction of Fig 4-11a is imaged with a sequential slice phase encode, it will be modulated with a k-space filter resembling the one in Fig 4-11b. The resultant image profile will look like Fig 4-11c.

By reordering the manner in which k-space is sampled, it is possible to reshape the effective k-space modulation filter [13]. Thus, by z phase encoding with a center out scheme, it is possible to apply to the object z profile shown in Fig 4-11d the effective k space modulation filter in Fig 4-11e. This results in the production of the image profile in Fig. 4-11f. It is apparent that although Fig 4-11f is blurred from the original object, it is much preferable in terms of amplitude and profile compared to Fig 4-11c. In the next section it will be shown that we can still further improve the



profile shown in Fig 4-11f by modulating the RF pulse amplitude through out the imaging segment.

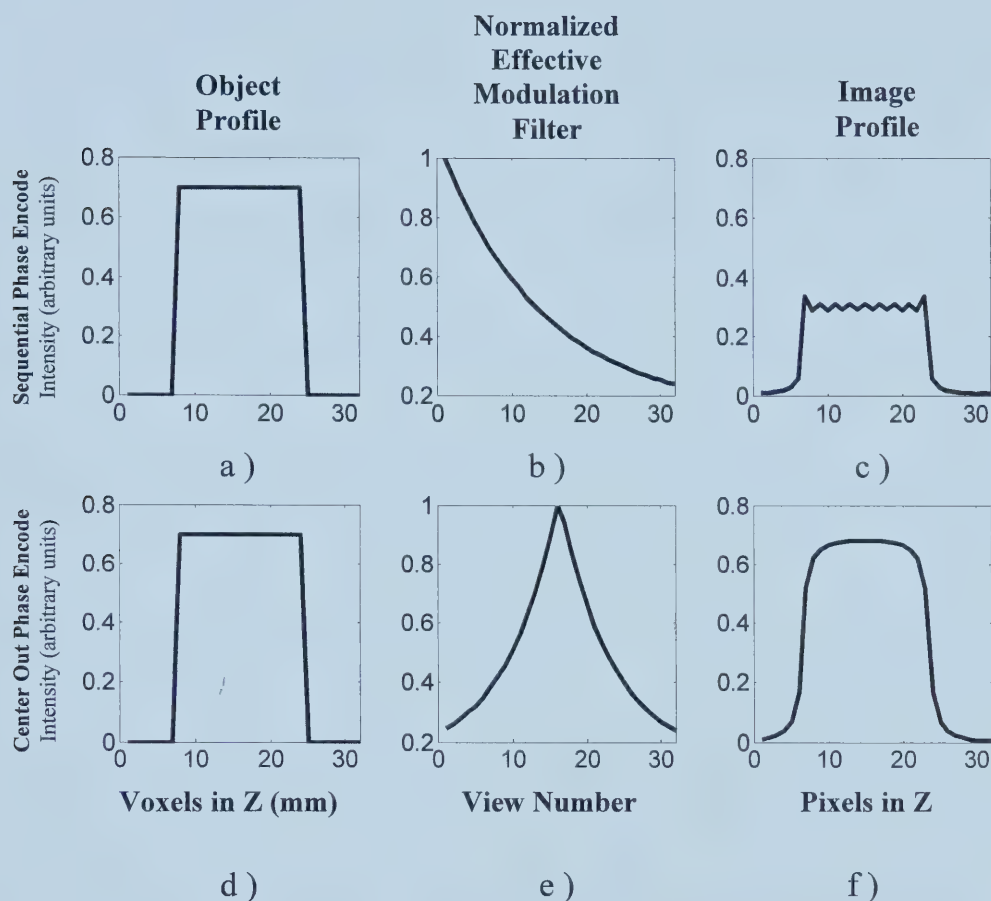


**Figure 4-11**

By changing the phase encode order, it is possible to reshape the k-space modulation function resulting from transient signal. (a-c) show the effect of a sequential slice phase encode with a FLASH data acquisition. (d-f) show the effect of a center out phase encode with a FLASH data acquisition. The model assumes a T1 of 1450 msec (blood) a TR of 10 msec a flip angle of 20° and no T2 dephasing.





### 4.33 Modulated Flip Angle for Modulating k Space

When subjected to short TR RF excitation of constant flip angle, the k space filter is the result of incomplete  $M_z$  relaxation between subsequent excitation pulses. Thus  $M_{xy}$ , when subjected to successive short TR RF pulses of given flip angle, decreases due to the fact that the  $M_z$  from which it samples decreases. It is however possible to increase the amount of  $M_{xy}$  sampled by increasing the RF flip angle [14]. This is only possible when there is sufficient relative availability of  $M_z$  following relaxation from the previous  $M_z$  evolution. To ensure adequate  $M_z$  through the later views it is often necessary to reduce the starting RF flip angle so that the initial  $M_z$  saturation is reduced. For this reason it is not possible to obtain static  $M_{xy}$  across all 32 views with a 10 msec TR and beginning with a  $20^\circ$  flip angle. Thus in order to maintain a relatively high center k space value, a starting value of  $15^\circ$  was used and the  $M_{xy}$  is not held constant but constrained to be 97.5 % of the previous value. This fraction is chosen because it is the maximum value for a starting flip angle of  $15^\circ$  that will effectively saturate  $M_z$  in 32views. Consequently a dramatic fall off would occur on the 33rd view as  $M_z$  is effectively used up. The Flip angle to be used for each view is determined with the equation:

$$\alpha_{(n)} = \text{SIN}^{-1} \left( \frac{[\text{SIN}(n-1) \bullet \text{SIN}(\alpha(n-1))] \bullet 97.5}{((M_z(n-1) \bullet \text{COS}(\alpha(n-1))) - M_0) \bullet \exp(-TR/T_1) + M_0} \right) \quad (4-2)$$



where  $n-1$  is the previous phase encode.

A comparison between 32 views acquired with a constant flip angle of  $20^\circ$  versus 32 views acquired with an increasing scheme is shown in Fig 4-12d. The resulting center out phase encode k space filters are shown in Fig 4-12 b,e respectively. The filter corresponding to a constant  $20^\circ$  flip angle has a higher initial signal followed by a relatively steep signal fall off until the final views have approximately 25% of the initial signal. The increasing flip angle scheme shows a lower center k space signal approximately 76% of the constant flip angle value. The signal fall off is more gradual with the increasing flip angle thus having higher signal for two thirds of the views. If the respective filters (shown in Fig 4-1 b,e) are applied to the object profile of Fig 4-11d, the resultant image profiles are shown in Fig 4-12 c,f. Fig 4-12f gives a lower intensity, but sharper image profile than the constant  $20^\circ$  flip angle scheme in Fig 4-12c.



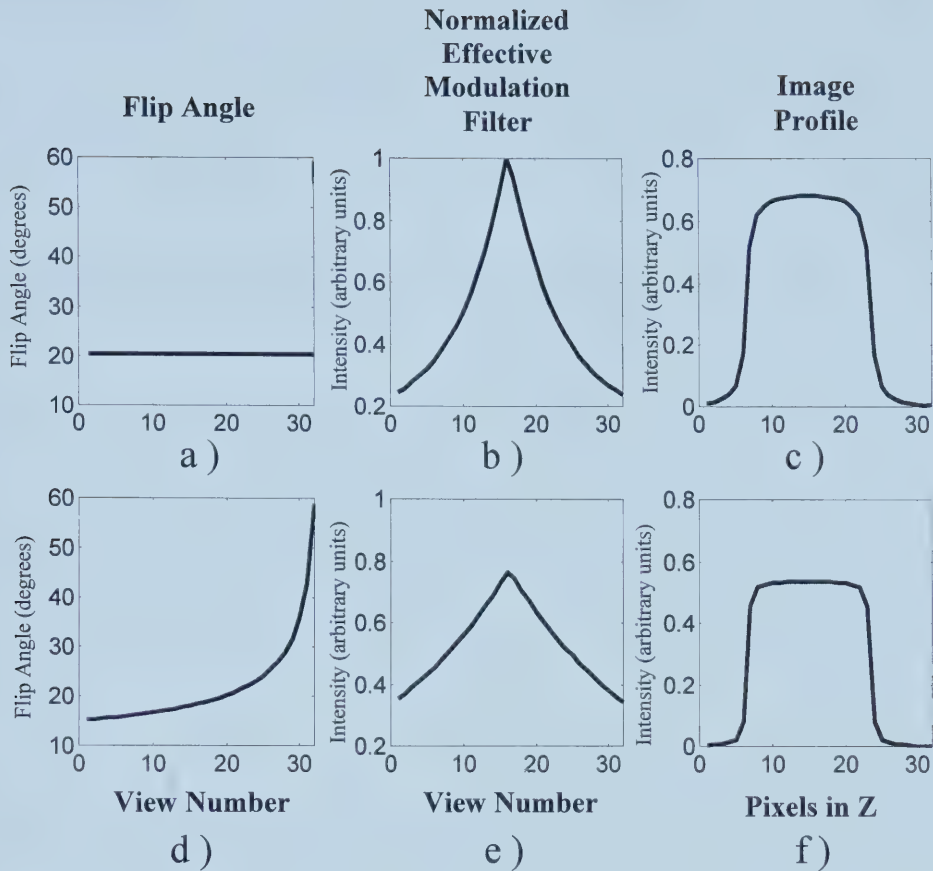


Figure 4-12

*It is possible to optimize the  $k$  space filter through modulation of the flip angle in order to produce a less blurred image. The model assumes a  $T_1$  of 1450 msec (blood) a  $TR$  of 10msec a flip angle of  $20^\circ$  and no  $T_2$  dephasing. See text for details.*

#### 4.4 Cardiac Triggering

For several reasons, cardiac triggering can improve the depiction of pulsatile anatomy such as the carotid arteries. A pulsatile vessel will move in conjunction with the cardiac cycle. Cardiac triggering allows the image to be acquired during the same portion of the cardiac cycle and thus the same physical position during the entire acquisition. Triggering also enables acquisition to occur during the diastolic part of



the cardiac cycle where there is less likelihood of complex or turbulent blood flow. This is especially important for patients with stenosis in which the flow may become especially complex [12,13,15]. The next section will talk about practical problems in regards cardiac triggering.

#### **4.41 Maximizing the T1 Advantage and the Two Heart Beat Acquisition**

In order to determine the null time for a given heart rate, a further constraint must be placed on the modeling of magnetization described in section 4.21. The constraint is that all the timings for a single complete segment must fit into an integer multiple of the interval between two subsequent heart beats (HBI). This can be imposed through the equation:

$$N' \cdot \text{HBI} = T_{\text{null}} + N \cdot \text{TR} + \text{Post image delay} \quad (4-3)$$

where  $N'$  is the number of heart beats over which the given imaging segment is acquired, and  $N$  is the number of phase encodes per image segment. Imposing this constraint allows for only one solution for any given heart rate and  $N'$  combination. For  $N'=1$  the solutions for the optimum  $T_{\text{null}}$  were graphed over a range of heart rates and for the experiment being carried at both 1.5 T and 3.0 T field strengths as shown in Fig. 13.





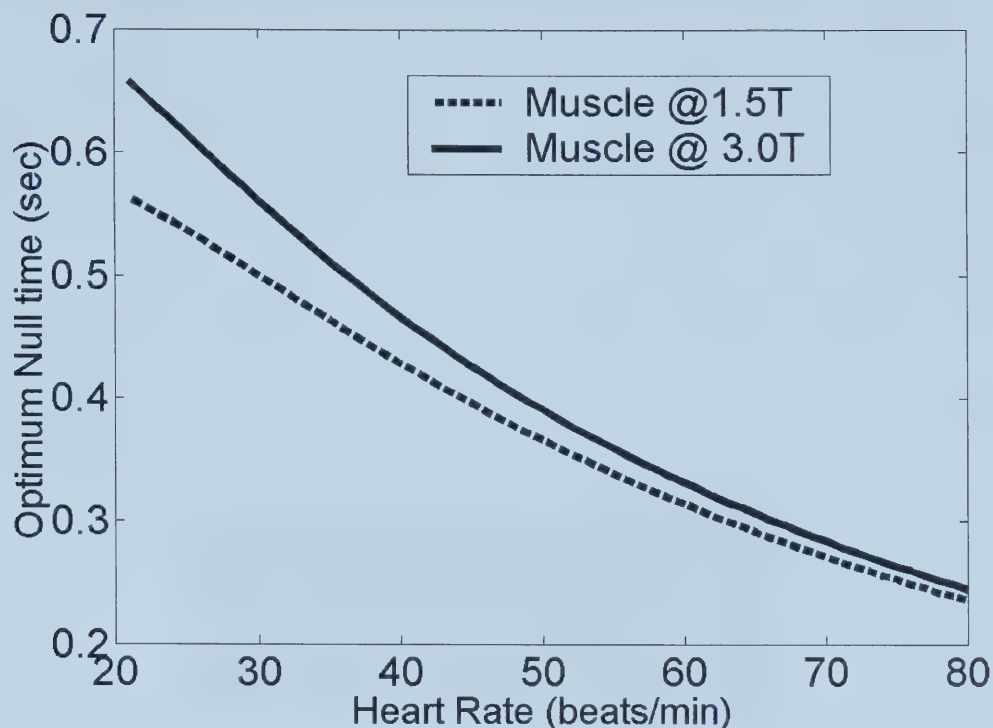


*Figure 4-13*

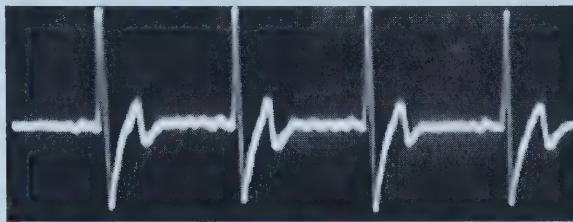
*Plot of optimal null time of muscle vs heart rate. The lines shown are for muscle at 1.5T ( $T_1=870$  msec) and 3.0T ( $T_1=1073$  msec).*

It is apparent that the relative increase in  $T_{\text{null}}$  at the higher 3.0 T field strength diminishes as heart rate increases. For this reason, a two heart beat interval acquisition was chosen to better exploit the 3.0 T advantage. Thus  $T_{\text{null}}$  for a  $N'=2$  acquisition will be the same as a  $N'=1$  acquisition with half the heart rate. The disadvantage to this technique is that by doubling  $N'$ , the image acquisition time is doubled.

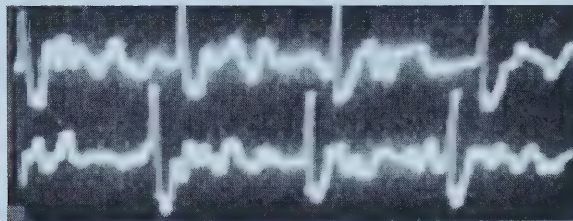


#### 4.42 Method of Cardiac Triggering (Electric vs Fiber Optic Leads)

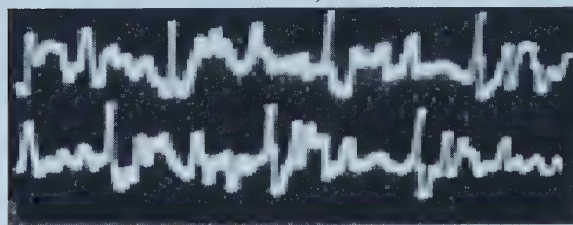
Initially the sequence was to be trigged with an electrocardiogram (EKG) using electric leads with the sequence triggering off the QRS complex. Although a clean signal could be obtained from the EKG of a volunteer outside the magnet (Fig 4-14a), the signal became substantially worse when the volunteer entered the magnet bore as a result of the magnetohydrodynamic effect (Fig 4 –14b) and even worse under the rigors of the imaging sequence (Fig 4 –14c) [16].



a )



b )



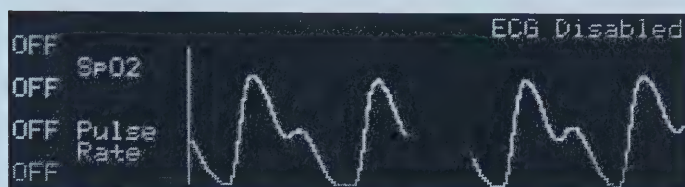
c )

*Fig 4-14*

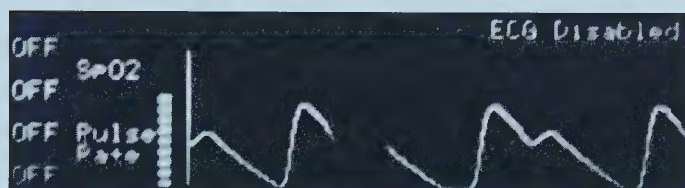
*a ) show a wave form from a volunteer outside the magnet, b ) shows the wave forms from a inside the magnet before imaging and c ) show the wave form during an imaging experiment.*



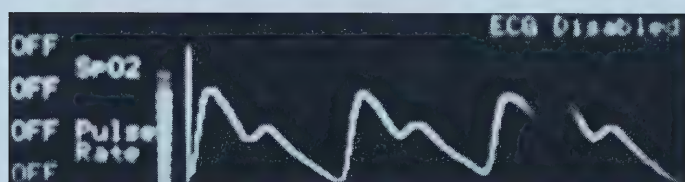
The waveform from a pulse oximeter (PO) with a fiber optic lead was found to be unaffected with respect to its regular outside the magnet performance Fig 4-15 a both in magnet with no imaging sequence running 4-15 b and in the magnet with an imaging sequence running 4-15c.



a )



b )



c )

*Figure 4-15*

*Shows the wave forms of the pulse oximeter a.) outside the magnet b.) within the magnet and c.) during an imaging sequence. Note change in wave form amplitude due to auto scaling by the oximeter and not a result of the magnetic field*



The pulse oximeter extrapolates heart rate by measuring changes in light absorption with the assumption that changes occur due to the variation in blood flow as result of the cardiac cycle. The sensor for this measurement is usually placed on the finger. As a result of this, there is a delay of approximately 480 msec between the QRS complex and the time the pulse oximeter detects the heartbeat. This time relates to the pulse wave velocity from the heart to the site of interest. If we take this into account and the fact that we do not want to be acquiring data into the second heart beat, the maximum heart rate that can have an effective  $T_{\text{null}}$  for a 32 view acquisition segment with 10 msec TR is approximately 73 beats per minute for an  $N'=2$  acquisition protocol.

#### **4.43 Positioning of the Inversion Pulse and Acquisition**

With cardiac triggering we wish to accomplish two things in terms of flow: First to maximize blood refreshment into the imaging slab, and second to. acquire the image during the slowest flow as to minimize ghosting and intravoxel dephasing. For a specific heart rate of 60 beats/min, in the proximal left common carotid, blood flow reaches a peak flow of 2500 cc/min approximately 150 msec after an EKG trigger, then slows to about  $1/5^{\text{th}}$  flow approximately 220 msec later climbing to approximately 1000 cc/min at approximately 460 msec after the EKG trigger than slowly tapers back to around 500 cc/min after about 600 msec [18]. Thus the optimum time for applying the inversion pulse is approximately 480 msec before the





next pulse oximeter trigger is expected to play out. The result of low flow imaging is a substantially less ghosted image shown in Fig 4-16.

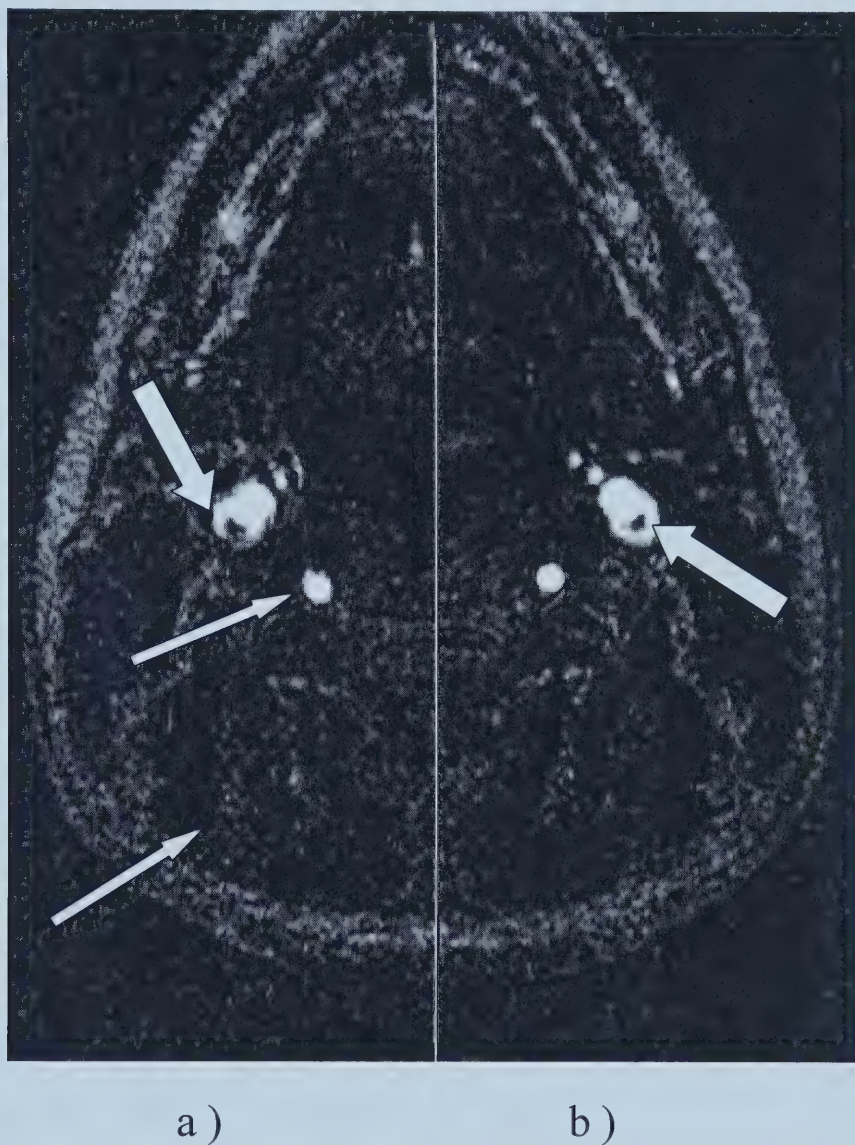


*Figure 4-16*

*Shows two images of the left side of the neck with the left side being reflected in the vertical dimension. The difference between the two halves is that a.) has been acquired without the addition of cardiac triggering and b.) has been acquired with cardiac triggering. Notice the vessel blurriness and ghosting (small white arrows) that exist without the addition of cardiac gating are substantially reduced with its addition. Big arrow shows signal drop out due to intra-voxel dephasing or incomplete blood refreshment between heart beats.*



#### **4.5 Comparison of MP TOF with Standard TOF**

Transverse scans using both 3D MP MRA and standard 3D TOF were run on 4 healthy volunteers with ages ranging from 21 to 23. The scans were run at the area of the bifurcation of the carotid artery. The images from both techniques were reconstructed in the same manner. Background measurements for SNR, CNR and Normalized Contrast were taken from 4 regions-of-interest (ROI) in the 17<sup>th</sup> slice of each slab. Blood signal measurements were taken from ROI within the vertebral arteries.

For MP MRA the Parameters are as follows: Flip angle =22 degrees, 32views per segment, TR/TE= 10/3.2 msec, Slab thickness=32 mm, FOV= 200 mm, Resolution = 512(x):256(y):32(z), BW =100 KHz oversampled 50% asymmetrical readout.  $T_{null}$  was dependant on the volunteers' heart rate. For TOF MRA the parameters are as follows: Flip angle =25, TR/TE=36/6.9 msec with flow compensation in the slice and read directions, Slab thickness= 32 mm, FOV= 200 mm, Resolution= 512(x):256(y):32(z), BW= 50 KHz oversampled 50% asymmetrical readout. A quadrature elliptical cervical neck transmit/receive coil (Medical Advances, Milwaukee) was used in both cases.

---



Table 4-1 shows a comparison of cardiac triggered (CT) MP MRA and TOF MRA in regards to SNR, CNR, Normalized Contrast (C) and Background signal to Noise (BNR) measurements

Table 4-1

Volunteer	MP MRA				TOF MRA			
	SNR	CNR	C	BNR	SNR	CNR	C	BNR
Case 1	31.9	29.7	13.4	2.2	50.4	40.6	4.15	9.8
Case 2	47.0	40.7	6.4	6.4	81.2	64.2	3.8	17.0
Case 3	27.6	25.3	11.1	2.3	38.3	30.2	3.7	8.1
Case 4	21.5	19.1	7.8	2.4	47.6	37.5	3.7	10.1

Table 4-2 shows the average percent change between TOF MRA and MP MRA using TOF MRA as the standard.

Table 4-2

SNR	CNR	C	BNR
-40% $\pm$ 11%	-32% $\pm$ 14%	<b>+150% <math>\pm</math> 72%</b>	-71% $\pm$ 6%



Although the background suppression is significantly higher in the MP MRA as shown in the BNR measurement, the higher noise associated with the cardiac triggered MP MRA affects the SNR and CNR measurements significantly.

Figure 4-17 shows a comparison between source images using both cardiac triggered MP MRA and TOF of the carotid and vertebral arteries superior to the bifurcation. Superior background is immediately noticeable in the CT MP MRA technique as compared to the TOF technique. Both half images show vessel blurring in the vertebral arteries.

Figure 4-18 shows a comparison between source images using both CT MP MRA and TOF of the carotid and vertebral arteries at the bifurcation. Vessel blurring of the vertebral artery apparent in the TOF MRA image is not apparent in the CT MP MRA. The carotid artery also appears less blurred in the MP MR although more intra voxel dephasing appears within the artery itself.







*Figure 4-17*

*A comparison between TOF MRA and MP MRA of the carotids and vertebral arteries just superior of the bifurcation of volunteer 1. Both images use 512x256x32 resolution with a 200 mm FOV and a 1 mm slice thickness.*





TOF MRA

MP MRA

*Figure 4-18*

*A comparison between TOF MRA and MP MRA of volunteer 3. Both images use 512x256x32 resolution with a 200 mm FOV and a 1 mm slice thickness.*



## 4.6 Discussion

Cardiac triggered MP MRA demonstrated much improved background suppression ( $-71\% \pm 6\%$ ) over TOF MRA, although it suffers from decreased SNR ( $-40\% \pm 11\%$ ). This is due to both lower flip angle and higher bandwidth readout of the MP MRA sequence. In comparing signal dropout due to intravoxel dephasing, no improvement was evident. This was most likely due to the fact that the volunteers used in comparisons were all healthy with excellent flow. In the case of stenosis, blood flow becomes increasingly complex with less vessel refilling. Under these conditions, cardiac gating should play an increasingly important role since the acquisition is limited to the diastolic period. Further improvements in terms of reduced intravoxel dephasing would also result if the TE could be further reduced. To accomplish this would require stronger and faster gradients which have now become increasingly common on state-of-the-art clinical scanners. For example the present work made use of 20 mT/m with a 100 T/m/s slew rate. The recently purchased Siemens Sonata system uses 40 mT/m with a 200 T/m/s slew rate which is a doubling in both strength and slew rate.

The longer T1 advantage which results from high field is only slightly realized in single heart beat acquisitions due to the short recovery time allowed within average to high heart rates. Two heart beat acquisitions are advantageous due to both the increased recovery and inflow times as well as the higher flexibility in inversion pulse placement.





Cardiac triggering devices with fiber optic leads appear necessary in order to maintain a reliable trigger. The delay of 480 msec in the pulse oximeters triggering signal also places an upper limit on heart rates in which the triggering will work. It is possible however to get around this by increasing the number of heartbeats in which a segment is sampled for higher heart rates.

In conclusion, we have developed the MP MRA technique at high field and tested it successfully on normal volunteers; however, further study as to its viability as compared to the TOF method for detection of carotid artery stenosis is warranted.





## 4.7 References

1. Potchen E, Haacke E, Siebert J, Gottschalk A. *Magnetic Resonance Angiography: Concepts and Applications*. St. Louis: Mosby, 1993.
2. Franck AF, Selby K, Tyen Rv, Nordell B, Saloner D. *Cardiac-gated MR angiography of pulsatile flow: k-space strategies*. J Magn Reson Img 1995;5:297-307.
3. Kim J, Sussman M, Huang Y, Westman D, Farb R, Pauly J, Nishimura D, Wright G. *Influence of Patient and Imaging Factors on Spatial Resolution of High Resolution 3D Gd-MRA of the Carotid Arteries*. 8th Ann Mtg, Int Soc Magn Reson. Denver: Int Soc Magn Reson, 2000:1231.
4. Nishimura DG, Macovski A, Pauly JM, Conolly SM. *MR angiography by selective inversion recovery*. Magn Reson Med 1987;4:193-202.
5. Wilman AH, Huston J, Riederer SJ. *Three-dimensional magnetization-prepared time-of flight MR angiography of the carotid and vertebral arteries*. Magn Reson Med 1997;37:252-259.
6. Edelman RR, Wallner B, Singer A, Atkinson DJ, Saini S. *Segmented TurboFLASH: method for breath-hold MR imaging of the liver with flexible contrast*. Radiology 1990;177:515-521.
7. Nishimura DG, Macovski A, Jackson JI, Hu RS, Stevick CA, Axel L. *Magnetic resonance angiography by selective inversion recovery using a compact gradient echo sequence*. Magn Reson Med 1988;8:96-103.



8. Edelman RR, Chien D, Atkinson DJ, Sandstrom J. *Fast time-of-flight MR angiography with improved background suppression*. Radiology 1991;179:867-870.
9. Richardson DB, Bampton AEH, Riederer SJ, MacFall JR. *Magnetization-prepared MR angiography with fat suppression and venous saturation*. J Magn Reson Img 1992;2:653-664.
10. Nishimura, D.G., *Principles of magnetic resonance imaging*. 1996: Stanford University.
11. Nagele T. *The effect of linearly increasing flip angles on 3D inflow MR angiography*. Magn Reson Med 1994;31:561-566.
12. Wilman AH, Riederer SJ, Grimm RC, Rossman PJ, Wang Y, King BF, Ehman RL. *Multiple breathold 3D time-of-flight MR angiography of the renal arteries*. Magn Reson Med 1996;35:426-434.
13. Wilman AH, Riederer SJ. *Improved centric phase encoding orders for three dimensional magnetization prepared MR angiography*. Magn Reson Med 1996;36:384-392.
14. Mugler JP, Epstein FH, Brookeman JR. *Shaping the signal response during the approach to steady state in three-dimensional magnetization-prepared rapid gradient echo imaging using variable flip angles*. Soc Magn Reson in Med. Berlin, 1992:431.



15. Li D, Haacke EM, Mugler JP, S.Berr, Brookeman JR, Hutton MC. *Three-dimensional time-of-flight MR angiography using selective inversion recovery RAGE with fat saturation and ECG-triggering: application to renal arteries.* Magn Reson Med 1994;31:414-422.
16. Chia JM, Fisher SE, Wickline SA, Lorenz CH. *Performance of QRS Detection for Cardiac Magnetic Resonance Imaging With a Novel Vectorcardiographic Triggering Method.* J Magn Reson Img 2000;12:678-688.
17. Bolster BD, Atalar E, Hardy CJ, McVeigh ER. *Accuracy of arterial pulse-wave velocity measurements using MR.* J Magn Reson Img 1998;8(4):878-888.
18. Bogren HG, Buonocore MH. *Blood flow measurements in the aorta and major arteries with MR velocity mapping.* J Magn Reson Img 1994;4:119-130.



## Chapter 5

### Conclusion

#### 5.1 Conclusions

In conclusion, this work has introduced two new pulse sequences at 3.0 T. First, a standard TOF MRA technique with the novel addition of pulsed magnetization transfer, and second, an inversion recovery magnetization-prepared MRA technique. Both sequences were developed and tested by the author, and the value of each method was demonstrated on normal volunteers.

We have demonstrated implementation of pulsed MT at 3.0 T for increased background suppression in TOF MRA. To accomplish this, the phase encode order was rearranged and run in conjunction with a modulated MT pulse amplitude. The result of this was that the center k-space views received higher amplitude MT pulses with edges receiving less MT. Further, MT pulse amplitude was temporally modulated such that over any 8 second period the average power was less than allowed by the FDA SAR limit of 3.0 W/kg. The results indicated that pulsed MT could be effective at 3.0 T without exceeding SAR limits and with normalized blood-to-background contrast improvements of approximately 50%.

We have also successfully developed cardiac triggered MP MRA at 3.0 T. We have demonstrated the advantages of the both higher field in relation to the magnetization





prepared component of the sequence and cardiac triggering. We have further shown that this method was successful in the imaging of normal volunteers with decreased background-to-noise ratio of approximately 71% over standard TOF MRA.

For both techniques, the stage is now set for further investigation into the detection of pathology in pulsatile vasculature via MP MRA and more constant flowing vessels via TOF MRA with pulsed MT.

## **5.2 Future Directions**

The immediate future direction for this work is to take the developed sequences for MT TOF MRA and MP MRA and begin to apply them to patient studies. In the present work these techniques have been applied solely to normal volunteers. Application to patient groups is now warranted. For MP MRA at 3.0 T, the technique could be applied for carotid bifurcation studies in patients with known stenosis. For TOF MRA, the technique would be useful for examining the intracranial vasculature in patients suffering from known vascular disease.

As well as patient studies, further work on TOF MRA could examine the ultimate resolution limits of TOF MRA at 3.0 T and whether phase array coil reception could further improve vessel visibility. For MP MRA, work could be done to increase SNR such as receiving with a surface coil. Localized 2D MP MRA or thin excitation slab 3D MP MRA might also be looked into. Advantages here will lie in a narrower spatial



inversion pulse which will allow greater blood refreshment than a thick slab, and fewer phase encodes to further shorten scan times.

The value of high field for MRA has been demonstrated in this work. The dual benefits of increased SNR and longer T1 times over 1.5 T have been beneficial. One obvious future direction is to extend the use of MRA to even higher field. In particular, the new 4.7 T system (arriving Sept. 2001) may allow even more effective MRA to be performed. Without MT, standard TOF MRA at 4.7 T should be possible owing to the low SAR of the low flip angle sequence. MT at 4.7 T may not be as effective due to the limitation of SAR and the low power amplifiers available at 4.7 T which may require much longer RF pulses to achieve effective MT, thus excessively lengthening the TR for TOF contrast. However with further optimization of a phase encode order and temporally modulated MT pulse amplitude, MT MRA may still provide improved background suppression over non-MT TOF MRA while maintaining FDA SAR limits. In terms of MP MRA, application at 4.7 T will not be limited by SAR. The MP MRA technique would also benefit from even further increases in T1 times at 4.7 T, allowing for greater inflow times for more complete blood refreshment.

















University of Alberta Library



0 1620 1467 4681

**B45568**